International Journal of Biological Macromolecules 207 (2022) 308–323

Contents lists available at ScienceDirect

International Journal of Biological Macromolecules

journal homepage: www.elsevier.com/locate/ijbiomac

Phage display identification of nanomolar ligands for human NEDD4-WW3: Energetic and dynamic implications for the development of broad-spectrum antivirals

Francisco Castillo [a,4], Carles Corbi-Verge [a,b,1], Javier Murciano-Calles [a], Adela M. Candel [a,2], Ziying Han [c], Manuel Iglesias-Bexiga [a,3], Javier Ruiz-Sanz [a], Philip M. Kim [b], Ronald N. Harty [c], Jose C. Martinez [a], Irene Luque [a,*]

[a] Department of Physical Chemistry, Institute of Biotechnology and Excelence Unit in Chemistry Applied to Biomedicine and Environment, School of Sciences, University of Granada, Campus Fuentenueva s/n 18071, Granada, Spain
[b] Donnelly Centre for Cellular and Biomolecular Research, Department of Molecular Genetics & Department of Computer Science, University of Toronto, Toronto, ON M5S 3E1, Canada
[c] Department of Pathobiology, School of Veterinary Medicine, University of Pennsylvania, 3800 Spruce St., Philadelphia, PA 19104, USA

ARTICLE INFO

Keywords:
NEDD4
WW domains
NEDD4-WW3 domain
Drug discovery
Polyproline recognition
Broad-spectrum antivirals
Phage display
Molecular dynamics simulations
Calorimetry
Nuclear magnetic resonance

ABSTRACT

The recognition of PPxY viral Late domains by the third WW domain of the human HECT-E3 ubiquitin ligase NEDD4 (NEDD4-WW3) is essential for the budding of many viruses. Blocking these interactions is a promising strategy to develop broad-spectrum antivirals. As all WW domains, NEDD4-WW3 is a challenging therapeutic target due to the low binding affinity of its natural interactions, its high conformational plasticity, and its complex thermodynamic behavior. In this work, we set out to investigate whether high affinity can be achieved for monovalent ligands binding to the isolated NEDD4-WW3 domain. We show that a competitive phage-display set-up allows for the identification of high-affinity peptides showing inhibitory activity of viral budding. A detailed biophysical study combining calorimetry, nuclear magnetic resonance, and molecular dynamic simulations reveals that the improvement in binding affinity does not arise from the establishment of new interactions with the domain, but is associated to conformational restrictions imposed by a novel C-terminal -LFP motif in the ligand, unprecedented in the PPxY interactome. These results, which highlight the complexity of WW domain interactions, provide valuable insight into the key elements for high binding affinity, of interest to guide virtual screening campaigns for the identification of novel therapeutics targeting NEDD4-WW3 interactions.

1. Introduction

WW domains are small protein-protein interaction modules that are found in more than 50 proteins in the human proteome and play key roles in cellular signal transduction. The enhancement or disruption of WW-mediated interactions has been proposed as a general strategy to develop novel treatments against the numerous diseases caused by dysregulated WW signaling. In fact, several WW domains are today well-established targets for drug design [1–4].

NEDD4 (neuronal precursor cell expressed developmentally down-regulated gene 4–1) is a HECT type E3 ubiquitin ligase widely expressed and evolutionarily conserved in eukaryotes. It is one of the nine members of the NEDD family of E3 ubiquitin ligases, characterized by a conserved modular architecture consisting of an N-terminal Ca^{2+} regulated C2 lipid-binding domain, two to four type I WW domains in charge of substrate recruitment through the recognition of peptide sequences containing a conserved PPxY core motif, and a C-terminal HECT catalytic domain. NEDD4 functions within the ubiquitin proteasome system

* Corresponding author at: University of Granada, Department of Physical Chemistry, School of Sciences, Campus Fuentenueva s/n 18071, Granada, Spain.
E-mail address: iluque@ugr.es (I. Luque).
[1] current address: Cyclica, 207 Queens Quay West, Suite 420, Toronto, Ontario, M5J 1A7, Canada
[2] current address: Eurofins Villapharma Research, S.L., Parque tecnológico de Fuente Álamo. Ctra. El Estrecho-Lobosillo, E30320, Fuente Álamo, Murcia, Spain.
[3] current address: Medical Department, Menarini S.A., C. dÁlfons XII, 587, 08918, Badalona, Spain.
[4] current address: MEDINA Foundation, Avevnida del Conocimiento 34, 18016 Granada, Spain.

https://doi.org/10.1016/j.ijbiomac.2022.03.010
Received 16 December 2021; Received in revised form 1 March 2022; Accepted 2 March 2022
Available online 5 March 2022

regulating trafficking and stability of signaling proteins implicated in multiple cellular processes, including sodium homeostasis, T-cell regulation, control of neuronal function as well as cellular growth and proliferation [5,6]. Even though NEDD4 contains four type I WW domains, most of its physiological interactions are mediated by its third WW domain (NEDD4-WW3), which is the main docking site for substrate recognition and a target for the development of novel therapeutics against diseases associated to NEDD4 abnormal activity, such as cancer, hypertension or neural disorders [7,8]. NEDD4 is also implicated in the progression of viral infection, playing an essential role in the budding process of numerous encapsulated viruses, including filoviruses (Ebola, Marburg), rhabdoviruses (Lassa), or arenaviruses (Rabies), through the interactions of NEDD4-WW3 with short and conserved PPxY-containing sequences present in the viral proteins, and known as Late or L-domains [9,10]. Blocking NEDD4-WW3/L-domain interactions has been shown to effectively inhibit budding in a number of viruses and has emerged as a promising strategy to identify novel, host-oriented, broad-spectrum antivirals with low susceptibility to the development of resistance [11–13].

The search for therapeutic agents based on the disruption/modulation of WW interactions requires the ability to develop high-affinity and specific ligands with good pharmacological properties. Unfortunately, over the years this has proven to be quite a challenging task, due to specific features of WW domains and their interactions that complicate the estimation of binding energetics from structure and, thus, rational design and ligand optimization.

In the first place, WW domains present shallow, featureless and highly adaptable binding sites. WW domains are the smallest β sheet fold in nature (30–50 amino acids), characterized by a stable three-stranded antiparallel β sheet structure [14,15]. They are named after two conserved tryptophan residues spaced 20 to 22 residues apart within the sequence: the first tryptophan lies on one side of the β sheet conforming a hydrophobic core important for domain stability, known as the "hydrophobic buckle"; the second tryptophan is part of a hydrophobic pocket at the binding site dedicated to proline recognition (the xP pocket), which is shared by other proline interaction modules such as SH3 and UEV domains [14,16]. WW domains have been classified in different specificity types according to the motifs they recognize [17]. Binding specificity between the different WW subfamilies is determined by a second binding site pocket, which in the case of type I WW domains is dedicated to the recognition of the Tyr residue in the PPxY consensus core-motif [18,19] (the xY pocket). Both xP and xY pockets are shallow and highly plastic, showing varying sizes and geometries in the different WW complexes that result in different orientations of the ligand on the surface of the domain. This conformational variability has been even observed between different complexes of the same domain. This is the case of NEDD4-WW3, which is a paradigmatic example of the extent of binding site conformational plasticity in WW domains [20].

Secondly, the interactions of WW domains with their natural partners are generally weak and relatively promiscuous [16,21], with dissociation constants typically in the mid-low μM range, although tighter complexes have been described for bidentate ligands binding to WW tandems [22–24]. Also, the binding energetics of peptide ligands to WW domains are dominated by strong enthalpy/entropy compensation effects: large differences are found in the magnitude of the binding enthalpies and entropies for different ligands that do not translate into changes in binding affinity, which remains quite homogeneous between the different WW domain complexes. Such enthalpy/entropy compensation effects are a major roadblock for the optimization of binding affinity [25].

Moreover, the binding affinities of WW domain ligands are not fully determined by the geometric and chemical characteristics of the ligand/domain interface [20]. On the contrary, as described for other polyproline recognition modules, such as SH3 [26] or UEV domains [27], WW domain interactions present characteristic thermodynamic profiles (markedly negative binding enthalpies partially compensated by unfavorable entropic contributions) that are inconsistent with the predominantly hydrophobic character of the binding interface and reveal a complex scenario that needs to be understood for successful rational design [20,28]. Additional factors, such as the presence of water-mediated interactions [29,30] or changes in the conformational distribution [31,32] and dynamic properties of the domain induced by ligand binding [33,34], have been shown to strongly influence the energetics of polyproline recognition.

In fact, it has been recently shown that major contributions to the binding energetics of WW domains arise from conformational effects. WW domains are the simplest and fastest folding all-β natural proteins and fold over small free energy barriers [35,36], being, thus, highly flexible. Our group has established that a set of WW domains, including NEDD4-WW3, are characterized by a downhill folding equilibrium, which entails broad native state ensembles that can be continuously modulated by changes in conditions, mutations, or ligand binding [37]. NEDD4-WW3 is the most paradigmatic example of downhill folding reported to date, showing the highest level of conformational flexibility and the smallest folding barrier. Along these lines, evidence has been provided by our group and others of coupling between the folding and binding equilibria for the NEDD4-WW3 domain [20,38,39], characterized by a highly adaptable binding site able to accommodate its ligands in different orientations through a conformational selection mechanism [20]. The plasticity associated to a conformationally heterogeneous native state is functionally relevant for NEDD4-WW3, dedicated to the recognition of multiple substrates, since it allows promiscuous binding as well as efficient modulation of the binding affinity and specificity with relatively minor changes in conditions. Nonetheless, it becomes an additional obstacle for the design of potent inhibitors.

All these features make of NEDD4-WW3, and, by extension most WW domains, extremely challenging targets for rational drug design, and raise questions about the feasibility of obtaining small drug-like ligands that could be of value as novel therapeutic agents: Is high binding affinity attainable for the binding of small monovalent ligands to isolated WW domains? Can the molecular determinants of high binding affinity be identified and ascribed to specific features within the ligand? Can these features be integrated into small-molecule inhibitors? In this work, we address these questions testing the ability of non-rational approaches, such as phage display, to overcome the limitations imposed by the energetic and conformational complexity of WW domains and produce tight-binding ligands with the ability to inhibit viral budding. With this purpose, we have set up a competitive phage display procedure that led to the identification of peptide sequences with submicromolar binding affinity for NEDD4-WW3, showing also inhibitory activity against the budding process of different viruses. The binding of these peptides to NEDD4-WW3 has been thoroughly analyzed using a combination of biophysical techniques including calorimetry, nuclear magnetic resonance, and molecular dynamic simulations. We find that high binding affinity originates from the conformational effects induced by a novel C-terminal -LFP motif in the ligand that translate into optimized intra- and intermolecular interactions. These results underline the potential of irrational approaches to exploit the complexity of WW domains, allowing for the identification of key and highly localized elements for high binding affinity that could be of interest to direct virtual screening campaigns for the identification of novel therapeutic agents targeting WW domain interactions.

2. Results

2.1. Competitive phage display identification of high-affinity ligands of NEDD4-WW3 with antibudding activity

A fully randomized 12-residue library was constructed at the multivalent pVIII protein of the M13 phage (pVIII-x_{12}) and screened against GST-NEDD4-WW3. After three rounds of selection and amplification, the best 25 colonies ranked by ELISA-antiM13 assays were

sequenced. As expected, all selected sequences contained the (L/P)PxY canonical core motif, characteristic of type 1 WW domain ligands [40,41] (Fig. 1A). To minimize the chelating effect and favor the identification of high-affinity sequences, pIII monovalent screening was performed fixing the (L/P)PxY core motif (pIII-x_5(L/P)PxYx_5). After four rounds of selection, the best 25 sequences presented a marked preference for Ser or Thr at the central position of the core motif (Fig. 1B). Also, a conserved LF(P/G) motif, not previously identified in natural ligands (Fig. 1D), clearly emerged at positions +3 to +5.

To better establish the preferences at poorly defined positions, a pIII-x_5(L/P)P(S/T)YxxLFP library was constructed. Expecting that this library could be enriched in high-affinity sequences, a more restrictive protocol was established for the last three rounds of selection, reducing the GST-NEDD4-WW3 concentration from 2 μM to 1 μM and imposing more stringent affinity requirements by screening against a pre-formed complex with the high-affinity P53BP2 peptide (Kd = 4.1 μM) [42,43]. This setup resulted in a significant reduction (3–5 orders of magnitude) in the number of bound phages. 24 single phage colonies were isolated from each round and tested by ELISA-antiM13. In most cases, a saturated ELISA signal was obtained, which precluded the identification of the best binders. To allow the discrimination of tight-binding sequences, a competitive ELISA assay was implemented using the P53BP2 peptide as a competing ligand. The best binders in the competitive ELISA assay showed a marked preference for Asp at position -5 and Glu at +2, defining an xDx(L/P)PSYxELFP motif (Fig. 1C). Positions -6 to -8 maintained a high variability, suggesting low relevance for binding affinity.

These binding preferences were incorporated into two novel peptide sequences with different core motif variants (PPSY and LPSY) expected

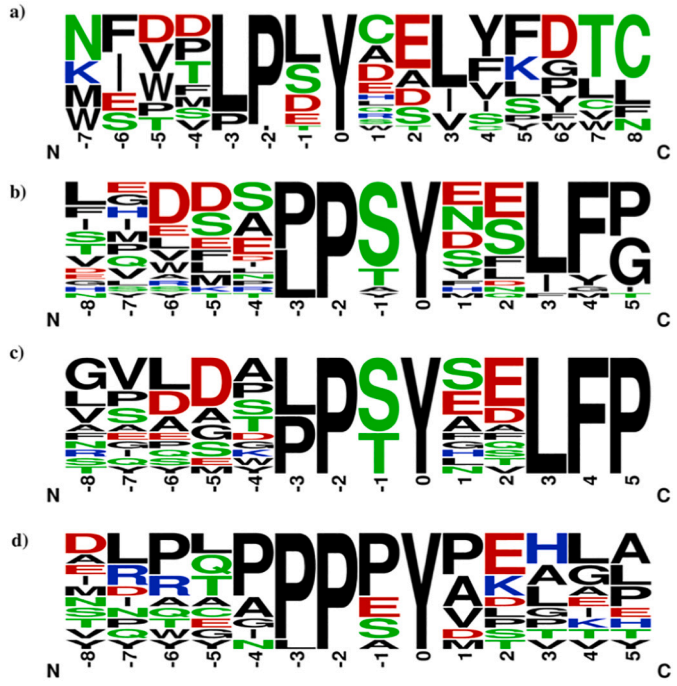

Fig. 1. Web-logo (https://weblogo.berkeley.edu) showing the frequency of occurrence of the different amino acids within the ligands selected by phage display (a) sequences derived from the fully randomized pVIII-x_{12} library; (b) sequences derived from the pIII-x_5L/PPxYx_5 library; (c) sequences derived from the pIII-x_5(L/P)P(S/T)YxxLFP library; (d) naturally-occurring sequences reported to bind NEDD4-WW3, including ligands P53BP2 (YPPYPPPPYPSGEP), HTLV-1 (SDPQIPPPYVEPTA), Ebola-VP40, Marburg-VP40 (MQYLNPPPYADHGA), Rabies-M2 (DLWLPPPEYVPLKE), EnaC (ALTAPPPAYATLGP), ARRDC3 (ERPEAPPSYAEVVT), dr-Comm (TIATGLPSYDEALH), Lats1a (VNRQPPPPYPLTAA), Lats1b (NYQGPPPPYPKHLL) and Lats2 (DRRCPPPPYPKHLL).

to bind NEDD4-WW3 with high binding affinity: LDAPPSYSELFP (UGR1) and LDSLPSYSELFP (UGR2). The binding energetics of UGR1 and UGR2 to NEDD4-WW3 were directly measured by ITC (Fig. S1). The resulting thermodynamic parameters are summarized in Table 1.

As expected, a significant improvement in binding affinity was achieved for both ligands, which bind to NEDD4-WW3 with a dissociation constant of 150 nM. This is, to the best of our knowledge, the tightest binding described for an isolated WW domain. It represents an improvement of one order of magnitude compared to the strongest binders reported to date for NEDD4-WW3 (P53BP2 and ARRDC3) and of two orders of magnitude compared with most natural ligands of this domain, including the viral Late domain sequences, which typically show dissociation constants in the 50 to 150 μM range [20,23,44].

The ability of the UGR ligands to inhibit viral budding in mammalian cells was tested using a well-established viral-like particle (VLP) assay [11,46,47]. To facilitate peptide translocation across the plasma membrane, a HIV-Tat internalization sequence [48] was attached to the N-terminus of UGR peptides, with negligible effect on the binding affinity (see Fig. S2). The Tat-UGR peptides at concentrations 10 to 30 μM produced a dose-dependent inhibition of VLP formation in the Marburg-VP40 (mVP40) and EbolaVP40 (eVP40) VLP assays, without deleterious effects on the cells (unaltered expression mVP40, eVP40 and actin) (Fig. 2A-B). The UGR peptides were also found to impair budding of live Vesicular Stomatitis Virus (VSV), which is contingent upon the interaction of the PPxY Late domain in the VSV-M protein and NEDD4 [11,49,50], confirming the disruption of the VSV-M/NEDD4 interaction in the context of a live virus (Fig. 2C).

2.2. *High-affinity for NEDD4-WW3 arises from highly favorable enthalpic contributions associated with the C-terminal LFP motif*

The UGR1 and UGR2 ligands present the thermodynamic signature characteristic of polyproline recognition (favorable binding enthalpies, opposed by unfavorable entropic contributions), but they show unusually large enthalpic contributions (-92 and -96 kJ·mol^{-1}, respectively) (Table 1). These values are well above those typically reported WW domain ligands (averaging 50–60 kJ·mol^{-1}), and close to the magnitude of the unfolding enthalpy of the NEDD4-WW3 domain itself (100 kJ·mol^{-1}) [37]. This enthalpic improvement is not counterbalanced by unfavorable entropic contributions being, thus, at the origin of the increment in binding affinity. Also, binding of these peptides induces large heat capacity changes (-2.2 kJ·(K·mol)$^{-1}$) that almost duplicate the values reported for other ligands ($\Delta C_{p,\ p53bp2/NEDD4\text{-}WW3}$ = -1.6 kJ·(K·mol)$^{-1}$ [20] and $\Delta C_{p,\ p53bp2/YAP\text{-}WW1}$ = -1.2 kJ·(K·mol)$^{-1}$ [28]).

The calorimetric analysis of a set of UGR1 derivatives reveals that the nanomolar binding affinity is associated with the C-terminal $L_{+3}F_{+4}P_{+5}$ motif (Table 1). Deletion of this LFP triad produced a large reduction in binding affinity (two orders of magnitude), binding enthalpy ($\Delta\Delta H_{UGR1\text{-}UGR1\Delta LFP}$ = -37 kJ·mol^{-1}) and binding heat capacity ($\Delta\Delta Cp_{UGR1\text{-}UGR1\Delta LFP}$ = -1.2 kJ·(K·mol)$^{-1}$), rendering a truncated ligand (UGR1-ΔLFP) with thermodynamic features very similar to other natural and low-affinity ligands, such as the Ebola or HTLV Late domains [20]. A Leu residue at position +3 has already been described as a high-affinity determinant for the binding of the ENaC and dr-Comm ligands to NEDD4-WW3, interacting with residues R_{855}, F_{857}, I_{859} at the so-called xL pocket in the WW domain, and stabilizing a helical turn in the ligand through the establishment of intra-molecular hydrogen bonds with Y_0 [44,45,51]. An equivalent role is played by a Val_{+3} residue in the ARRDC3 complex, which, in this case, induces a 3_{10} turn in the ligand [23]. Interestingly, these helical conformations are not observed in the low-affinity Ebola and HTLV1 Late domain complexes that lack an aliphatic residue at position +3 and adopt more extended conformations in the complex structures [20]. Nonetheless, L_{+3} alone does not suffice to achieve submicromolar binding affinities, since replacing the C-terminal FP residues with other amino acids less frequently observed in the phage display experiments (UGR1-YG) reduces binding affinity by one order of

Table 1
Binding energetics of peptide ligands to NEDD4-WW3.

Ligand	Sequence	Kd (μM)	ΔG_{ap} (kJ·mol^{-1})	ΔH_{ap} (kJ·mol^{-1})	$-T\cdot\Delta S_{ap}$ (kJ·mol^{-1})	ΔC_p (kJ/(K·mol)$^{-1}$)
UGR1	LDA**PPSY$_0$**SEL$_{+3}$FP	0.15±0.01	-38.2±0.2	-92.0±0.3	57.8±0.5	-2.2±0.1
UGR2	LDS**LPSY$_0$**SEL$_{+3}$FP	0.15±0.01	-38.2±0.2	-96.0±0.5	53.8±0.7	-2.0±0.1
UGR1-ΔLFP	LDA**PPSY$_0$**SE	25±2	-25.7±0.2	-55±2	29±2	-1.0±0.1
UGR1-E2S	LDA**PPSY$_0$**SSL$_{+3}$FP	0.26±0.03	-36.7±0.4	-79.8±0.6	43.1±1.0	–
UGR1-LYG	LDA**PPSY$_0$**SEL$_{+3}$YG	0.92±0.07	-34.1±0.3	-61.0±0.5	26.8±0.8	–
UGR1-ΔN	SEL$_{+3}$FP	n.b[a]	–	–	–	–
P53BP2 [20]	EYPPYP**PPPY$_0$**PSG$_{+3}$	5.3	-30.1	-53.2	23.1	–
ARRDC3 [23]	ERPEA**PPSY$_0$**AEV$_{+3}$VTE	3.3	-31.3	-75.4	44.1	–
ENaC [44]	TAP**PPAY$_0$**ATL$_{+3}$G	44.5	-24.8	-58.2	33.4	–
dr-Comm [45]	TG**LPSY$_0$**DEA$_{+3}$LH	3.0	-31.5	–	–	–
HTLV1 [20]	SDPQI**PPPY$_0$**VEP$_{+3}$	61.0	-24.1	-68.2	44.1	–
Ebola [20]	ILPTA**PPEY$_0$**ME	146.9	-21.9	-50,7	28.8	–
Ebola-long	ILPTA**PPEY$_0$**MEA$_{+3}$IYP	75.8±0.9	-23.5±0.1	-78.9±0.4	55.4±0.3	–

ITC experiments were performed at 25 °C in 20 mM sodium phosphate buffer at pH 7.0. Error values correspond to the best fitting of the experimental data to the one binding site model as implemented in Origin's Microcal LLC ITC ® Software.
[a] n.b.: no binding detected.

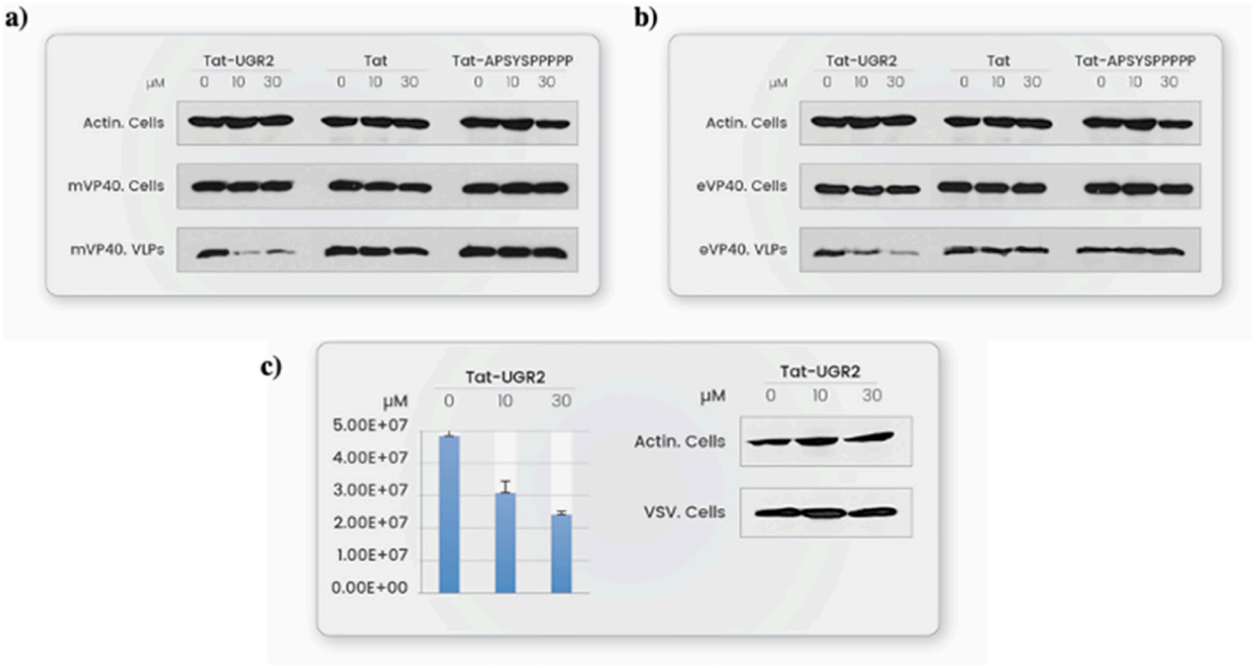

Fig. 2. Effect of UGR peptides on the PPxY-dependent budding of enveloped viruses. **(a-b)** HEK293T cells transfected with mVP40-pCAGGS vector **(a)** or eVP40-pCAGGS vector **(b)** were treated with the indicated concentrations of Tat-UGR2 (lanes 1–3), or negative controls (Tat, lanes 4–6; Tat-APSYSPPPPP, lanes 7–9). Cells and VLPs were harvested at 24 h post-transfection. A representative Western blot to detect mVP40 is shown; (**c**) HEK293T cells were infected with VSV-M virus at an MOI of 0.1 in the presence of 0, 10 and 30 μM of Tat-UGR2. Supernatants were harvested at 8 h post-infection, and virions were quantified by standard plaque assay on BHK-21 cells performed in triplicate and graphed as PFU/mL. VSV virus production in cell was also quantified by Western blot. For each Western blot experiment, constitutive β-actin in cells is shown as control.

magnitude, to the levels of the ARRDC3 ligand. This suggests that this newly identified FP dyad is a key element for tight binding, being responsible for 85% of the loss in binding enthalpy associated with the removal of the LFP motif.

2.3. The C-terminal LFP triad on the UGR ligands modulates the conformational dynamics of NEDD4-WW3 domain

To gain further insight into the mechanisms by which the LFP motif leads to such remarkable thermodynamic effects, $^{1}H—^{15}N$ HSQC titration experiments were performed with the high-affinity UGR1 and UGR2 ligands and their truncated variants UGR1-ΔLFP and UGR2-ΔLFP (Figs. S3 and S4). Under saturating conditions, all ligands induced perturbations in the same set of residues, suggesting that the submicromolar binding affinity of UGR1 and UGR2 does not result from new interactions in additional pockets in NEDD4-WW3. The Chemical Shift Perturbation (CSP) profiles of the UGR1-ΔLFP and UGR2-ΔLFP ligands closely resemble those reported for other low-affinity natural ligands, such as ENaC [38], Ebola, or HTLV1 [20] (Fig. S5). Nonetheless, as shown in Fig. 3, the introduction of the LFP triad results in significant changes in the magnitude of the CSPs for a small set of residues: i) E_{847}, V_{848}, and R_{849} at the β1 strand, not in direct contact with the ligand ii) F_{857} and F_{858} at the β2 strand: the first located at the base of the xP pocket and the second directed at the opposite site of the β-sheet and implicated in the hydrophobic buckle essential for domain stability; and iii) I_{859} and T_{866}, delimiting the xP and xY pockets and previously identified as essential elements for WW binding site plasticity [20].

The LFP triplet also has a profound impact on the nature of the chemical exchange processes. In the truncated UGR1-ΔLFP and UGR2-ΔLFP complexes, all residues not directly implicated in binding are

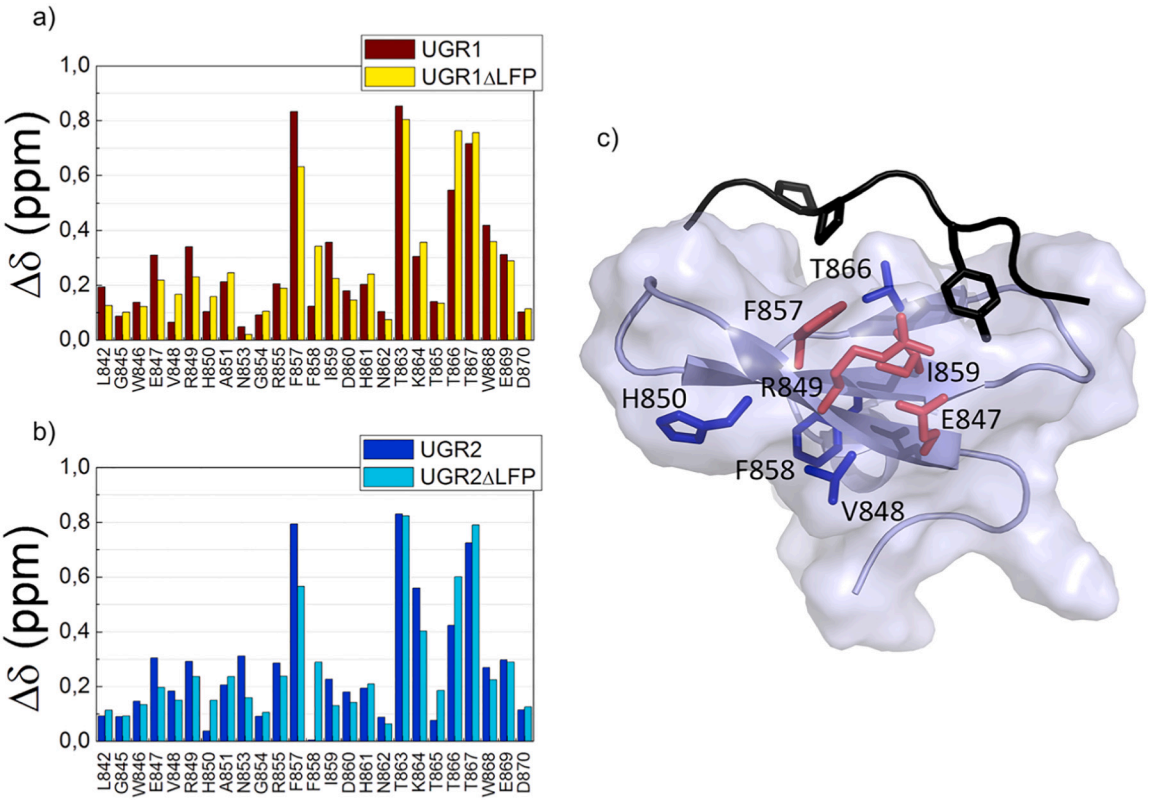

Fig. 3. Chemical shift perturbation of the NEDD4-WW3 backbone amide signals (weighted average for ^{1}HN and ^{15}N at the last titration point) caused by the presence of UGR1 **(a)** and UGR2 **(b)** ligands in comparison with their truncated versions UGR1ΔLFP and UGR2ΔLFP. **(c)** Mapping of the residues with the largest chemical shift differences upon truncation of UGR1 on the structure of the NEDD4WW3/Ebola complex (2KQ0). Residues incrementing CSP upon truncation are shown as red sticks and residues experiencing a CSP reduction as blue sticks. As a reference, the Ebola ligand is shown as a black ribbon, with critical PPxY residues in the core motif shown as black sticks. (For interpretation of the references to colour in this figure legend, the reader is referred to the web version of this article).

found in the fast exchange regime and most interacting residues in intermediate regimes (Fig. 4A), in agreement with previous reports for other NEDD4-WW3 ligands (αENaC [38], Ebola or HTLV1 [20]). In contrast, the binding of UGR1 and UGR2 induces a massive change in the behavior of the NEDD4-WW3 domain, so that a high percentage of the observed residues now shift to the slow-exchange regime (59% and 54% for UGR1 and UGR2 respectively) (Fig. 4B). Many of these slow-exchanging amino acids are located in the β1 and β2 strands and include those residues associated with the highest CSP values, some of them not in direct contact with the ligand. These effects extend to the β1-β2 and β2-β3 loops and are also transmitted to distant regions from the binding site, including the highly flexible N- and C-terminal tails.

The strong impact of the UGR ligands on the conformational distribution of the hNEDD4-WW3 domain is further illustrated by the large increase in cooperativity observed in the DSC profiles that shift from the extremely broad transitions characteristic of the free domain and compatible with a downhill folding equilibrium [37], to sharp and highly cooperative traces for the UGR complexes, which conform to a fully cooperative two-state model (Fig. 4C). In fact, the unfolding enthalpy (ΔH_{Tm} = 206 kJ·mol^{-1}) and the stability ($\Delta G_{25°C}$ = 12.3 kJ·mol^{-1}) of the NEDD4-WW3/UGR complex duplicates that of the free domain, being now comparable to the values typically displayed by other well-folded protein domains of similar size, such as SH3 domains [52].

2.4. The LFP triad rigidifies the ligand and improves the packing of the PPxY core against the NEDD4-WW3 domain

To further understand the impact of the LFP triad on the conformational properties of the NEDD4-WW3 complexes, a structural model of the NEDD4-WW3/UGR1 complex was generated using the crystal structure of the ARRDC3 complex (4N7H) as a template [23] (Fig. 5). 150 ns Molecular Dynamics trajectories of the UGR1 complex and the UGR1ΔP, UGR1ΔFP, and UGR1ΔLFP deletion variants were calculated from three independent 50 ns replicas. As a reference, equivalent simulations were performed for all available structures of NEDD4-WW3 complexes (ARRDC3:4N7H, ENaC:2M30, dr-Comm:2EZ5, HTLV1:2KPZ, and Ebola:2KQ0). In all cases, the backbone root-mean-square deviation (RMSD) rapidly reached a plateau at about 2 Å without abrupt transitions in the energy profile, indicating that the WW domains remained folded and stable throughout the simulations. The RMSF profile of the hNEDD4-WW3 domain is similar for all complexes, except for the ENaC and HTLV1 NMR structures that show a higher level of flexibility at the β1-β2 and β2-β3 loops (Fig. S6-B), in agreement with previous reports [20,44]. The ligands show different behaviors: UGR1 is more rigid (RMSF values ≤1 Å for the A_{-4}-L_{+3} region) and the flexibility progressively increases upon removal of the P_{+5}, F_{+4}, and L_{+3} residues, with UGR1ΔLFP reaching fluctuation levels (RMSF values ≥3 Å), similar to those of the Ebola and HTLV1 ligands (Fig. S6-A).

Analysis of the MD trajectories reveals that neither F_{+4} nor P_{+5} in UGR1 participate in any persistent contacts with NEDD4-WW3 (the C_β-C_β distance between these residues and the domain remains above 12 Å at all times). The simulations show, nonetheless, that these two bulky and conformationally constrained residues exert a marked effect on the conformational behavior of the ligands that translates into changes in the intra- and intermolecular interactions, underlying the strong energetic effects associated with the LFP triad.

In this way, while the core-motif prolines (P_{-3} and P_{-2}) show a very homogeneous behavior in all complexes adopting well-defined PPII geometries, the conformational preferences of residues C-terminal from

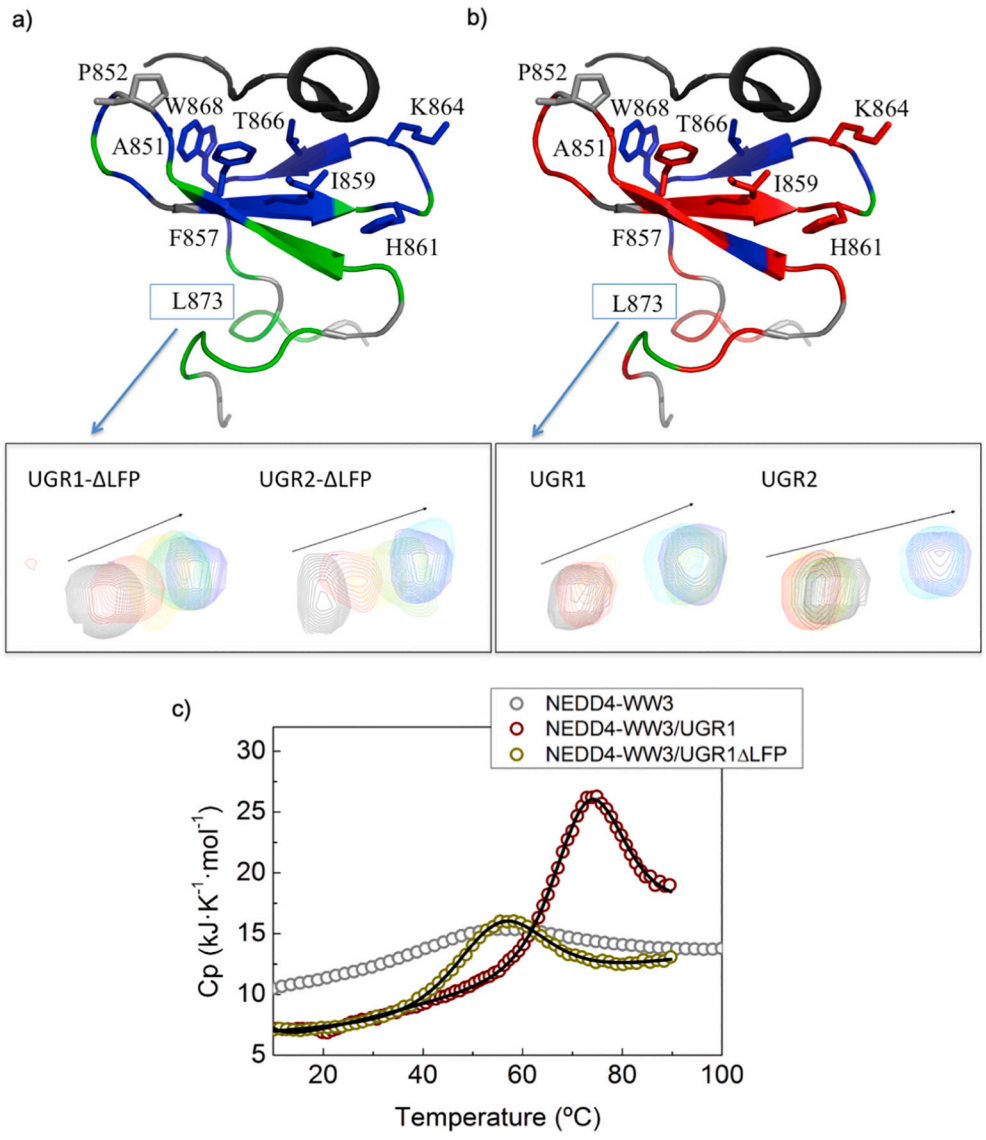

Fig. 4. Modulation of NEDD4-WW3 conformational behavior upon ligand binding. Mapping of the chemical exchange regime (green: fast exchange; blue: intermediate exchange; red: slow exchange) of the NEDD4-WW3 residues upon binding of the UGR1 **(a)** and UGR1ΔLFP **(b)** ligands. The insets illustrate, as an example, the differential behavior of residue L873 at the NEDD4-WW3 C-terminus, distant from the binding site. **(c)** Differential Scanning Calorimetry thermal denaturation profiles of NEDD4-WW3 free (grey) and in complex with UGR1 (wine) and UGR1ΔLFP (yellow). Symbols correspond to the experimental data for the temperature dependency of the partial molar heat capacity at pH 7.0. Solid red lines correspond to the best fit to a two-states thermodynamic model. (For interpretation of the references to colour in this figure legend, the reader is referred to the web version of this article).

Y_0 are more variable and strongly influenced by the nature of residues at positions +3 to +5 (Fig. 6 and Table S1). In agreement with previous reports [23,44], those ligands (ARRDC3, ENaC, and UGR1ΔFP) with a Leu residue at +3 adopt α or 3_{10} helical conformations in the Y_0-L_{+3} region with high frequency (40–60% of the simulation time). A similar behavior is observed for the dr-Comm ligand, containing an Ala_{+3}-Leu_{+4} combination of highly helical prone residues. In the case of UGR1, a 20% increment in the occurrence of helical conformations, up to 80% of the simulation time, is observed, associated with the strong conformational restrictions imposed by P_{+5} on F_{+4}, and subsequently on L_{+3} (Fig. 6A). The $F_{+4}P_{+5}$ dyad drives the conformational equilibrium towards α-helical structures, which are predominant in UGR1 (>50%), reduced upon removal of P_{+5} (24%), and completely replaced by 3_{10} helices in UGR1ΔFP, which shows a conformational behavior very similar to the ARRDC3 or ENaC ligands (Fig. 6B). Removal of L_{+3} in UGR1ΔLFP completely abolishes the formation of stable secondary structure elements, producing more extended structures and a higher conformational dispersion, as observed for the Ebola and HTLV1 ligands.

The C-terminal Y_0-L_{+3} helical turns in the different ligands are stabilized by highly populated intra-molecular hydrogen bonds between Ser_{-1} at the central position of the PPxY motif and Glu_{+2}. Both residues were strongly selected at these positions from the phage-display library containing the -LFP motif (see Fig. 1). These include: a) a hydrogen bond between the carbonyl oxygen of Ser_{-1} and the amide nitrogen of residues at position +2 (Glu/Thr) or, less frequently, at position +3 (Leu/Ala/Val) and b) two additional hydrogen bonds implicating Ser_{-1} and the side chain atoms of Glu_{+2} (Thr_{+2} in dr-Comm) (Fig. 7B). The frequency of occurrence of these hydrogen bonds in the UGR1 ligand is reduced between 10 and 15% upon removal of the FP dyad and dramatically drops when the full LFP motif is eliminated.

The stability of the Y_0-L_{+3} helical conformation influences the formation of intermolecular hydrogen bonds between the ligand and the NEDD4-WW3 domain. Two highly populated hydrogen bonds are observed in the UGR1 complex implicating the carbonyl oxygens of ligand residues D_{-5} and P_{-2} and the side chains of W_{868} and T_{866} at the xP pocket (Fig. 7C). These two hydrogen bonds are found in all other complexes, being highly populated for those ligands presenting Y_0-L_{+3} helical conformations and rare (occupancies <25%) for the Ebola and HTLV1 complexes, which show a different and more dispersed pattern of hydrogen bonds. The UGR1 LFP triad does not influence the D_{-5}/W_{868} interaction, but it affects the P_{-2}:O/T_{866}:Oγ hydrogen bond: 83% occurrence for UGR1 that is reduced by 10% upon removal of the FP dyad (to the levels of the other helix-forming ligand ARRDC3, ENaC, and dr-Comm), and by 30% in the absence of the full -LFP motif.

Packing of Y_0 at the xY pocket is optimal for L_{+3}–containing ligands (ENaC, dr-Comm, UGR1, UGR1ΔP, and UGR1ΔFP), but does not seem to

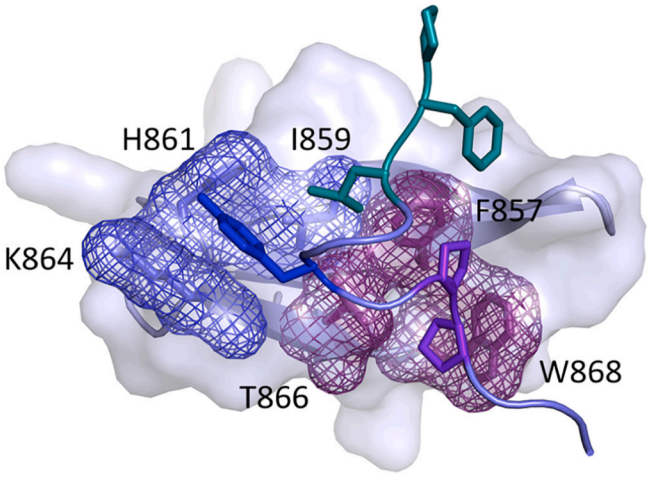

Fig. 5. Structural model of the UGR1/NEDD4-WW3 complex. The xP (wine) and xY (blue) pockets at the binding site are highlighted as a mesh representation on the surface of the NEDD4-WW3 domain and the UGR1 ligand is shown as a ribbon. The most relevant residues in UGR1 are shown as colored sticks: $P_{-2}P_{-3}$ (violet), Y0 (blue) and the $L_{+3}F_{+4}P_{+5}$ motif (dark cyan). (For interpretation of the references to colour in this figure legend, the reader is referred to the web version of this article).

be strongly influenced by the presence of the FP dyad (Fig. 7A, right panel). The situation is different for the interactions at the xL pocket (F_{857}, I_{859} and T_{866}), which are only observed for those ligands adopting a helical turn at the Y_0-L_{+3} region, since the more extended conformations, predominant for HTLV1, Ebola, or UGR1ΔLFP, place the C-termini far from this region. In this case, the conformational effects imposed by the $F_{+4}P_{+5}$ dyad strengthen L_{+3} interactions with residues F_{857} and T_{866} at the xL pocket (Fig. 7A, left panel). In the case of the L_{+3}-T_{866} interaction, the average distance in the UGR1 simulation is significantly reduced (up to 6 Å smaller) compared to all other helix-forming ligands (ENaC, dr-Comm, UGR1ΔP or UGR1ΔFP).

2.5. The LFP triad enhances the effect of ligand binding on NEDD4-WW3 intramolecular interactions and dynamics

The effect of the -LFP motif propagates throughout the domain structure, inducing changes in the frequency of occurrence of WW intradomain hydrogen bonds that extend to the N- and C- terminal ends of the domain (Fig. S7A). The effects on hydrogen bond occupancy are subtle to moderate (between 5 and 15%) for the backbone interactions (Fig. S7B) but become more significant (> 25%) for some side chain hydrogen bonds (Fig. S7C). This is the case of the interactions implicating the side chains of E_{847} and R_{849} as well as the backbone atoms of V_{848} at the first β strand, located between 6 and 14 Å away from the ligand in the model structure. In the UGR1 complex, the R_{849} side chain is engaged in long-lived intramolecular hydrogen bonds with the Oε atoms of the E_{857} side chain (60% of the simulation time) and the carbonyl oxygen of V_{848} (20%). These interactions are rare (<10%) in the UGR1ΔLFP simulation, where an E_{857}: Oε -V_{848}:N hydrogen bond becomes predominant. Additionally, changes in the average contact distance (up to 0.4 Å) are observed for the interactions established by the C-terminal P_{871} with other residues (P_{843}, W_{848}, F_{858}) in the hydrophobic buckle, key for the stability and cooperativity of the WW domain (Fig. S6D).

These observations suggest that the -LFP motif could be modulating the effects of ligand binding on the conformational dynamics of the NEDD4-WW3 domain and that such changes could be at the origin of the large energetic effects elicited by the LFP triad. Considering that large-scale structural fluctuations are not easily captured on the time scale accessible for our all-atom MD simulations, the equilibrium dynamics of the free domain, the UGR1 and UGR1-ΔLFP complexes were studied using coarse-grained Normal Mode Analysis (NMA) [53,54]. This study confirms that binding of the ligand has a strong impact on the overall dynamics and cooperativity of the NEDD4-WW3 domain, as indicated by the NMR and DSC results. This is illustrated in Fig. 8, showing the effects of UGR1 binding on the degree of correlation between the movement of the different residue pairs in the NEDD4-WW3 domain. In the free domain strong correlations between residues are mostly associated with trivial connections between contiguous amino acids and adjacent secondary structure elements (see the contact map in Fig. 8 as a reference), while correlations between distant elements in the domain, including the N- and C-terminal tails, are scarce and relatively weak. The presence of the ligand strengthens long-range couplings throughout the domain and enhances concerted motions of regions that were poorly correlated in the absence of the ligand. These include, in good agreement with the MD and NMR results: a) residues conforming the hydrophobic buckle, such as P_{871}, P_{843}, and W_{846}; b) binding site residues, such as K_{864} and T_{866} at the xY pocket; c) residues E_{847}, V_{848} and R_{849} at the β1 strand; and d) the highly flexible N- and C-terminal tails, now strongly connected with each other and with all β strands and loops in the domain.

The increase in cooperativity upon ligand binding is also apparent in the perturbation/response matrices derived from the NMA simulations (see Figs. S8, S9 and S10 for the free domain, the UGR1ΔLFP complex and the UGR1 complex respectively). In both complexes, perturbations at distal N- and C-terminal residues induce strong responses throughout the domain structure, which are not observed for free NEDD4-WW3, including residues at the hydrophobic buckle (P_{843} or P_{871}) and the binding site, such as K_{864} (xY pocket), T_{866} (xY, xP and xL pockets) and W_{868} (xP pocket). The presence of the -LFP triad further modulates the perturbation/response patterns. For example: a) it increases the response of the ligand $PPSY_0$ core motif to the domain N- and C- termini; b) for the UGR1 complex, perturbations at the residues +1 to +5 in the ligand elicit strong responses in binding site and hydrophobic buckle residues that are not produced in the truncated UGR1ΔLFP complex; and c) the responses of residues W_{846} (hydrophobic buckle), E_{847}-V_{848}-R_{849} (β1), and P_{856}-F_{857} (β2) to perturbations at the β1-β2 loop are also enhanced. Of special interest are the effects induced by the -LFP triad on residues T_{866} and I_{859} at the binding site. The response of T_{866}, implicated in the xP, xY. and xL pockets, to perturbations at other binding site residues (I_{859}, H_{861}, or W_{868}) is weak in the truncated complex but becomes very strong in the presence of the -LFP triad. In turn, the -LFP motif does not affect the response of I_{859} to other binding site residues (very strong in both complexes) but significantly increases its response to most residues in the hydrophobic buckle (W_{846}, F_{858}, and P_{871}).

These results are in excellent agreement with the changes in hydrogen bond and contact distances observed in the all-atom MD simulations and the experimental NMR results, showing that the effects of the -LFP motif on the ligand/domain interactions are mostly mediated through T_{866}, which shows the strongest NMR-CSP differences (Fig. 3), enhanced intermolecular hydrogen bonds with P_{-2}, and improved packing at xL pocket (Fig. 7). These effects seem to be relayed to the NEDD4-WW3 domain through the interplay between T_{866} and I_{859}, affecting different regions of the domain, including the hydrophobic buckle, key for domain stability and cooperativity.

3. Discussion

The massive screening of large peptide libraries by phage-display has allowed us to identify high-affinity ligands for the NEDD4-WW3 domain, overcoming the difficulties inherent to WW domain recognition. The 150 nM dissociation constants of our UGR peptides are, to the best of our knowledge, the highest binding affinities reported for an isolated WW domain (between 1 and 2 orders of magnitude higher than other ligands). These results prove that high binding affinity is attainable for the recognition of monovalent ligands by isolated WW domains, even though these domains have evolved to mediate weak and transient interactions.

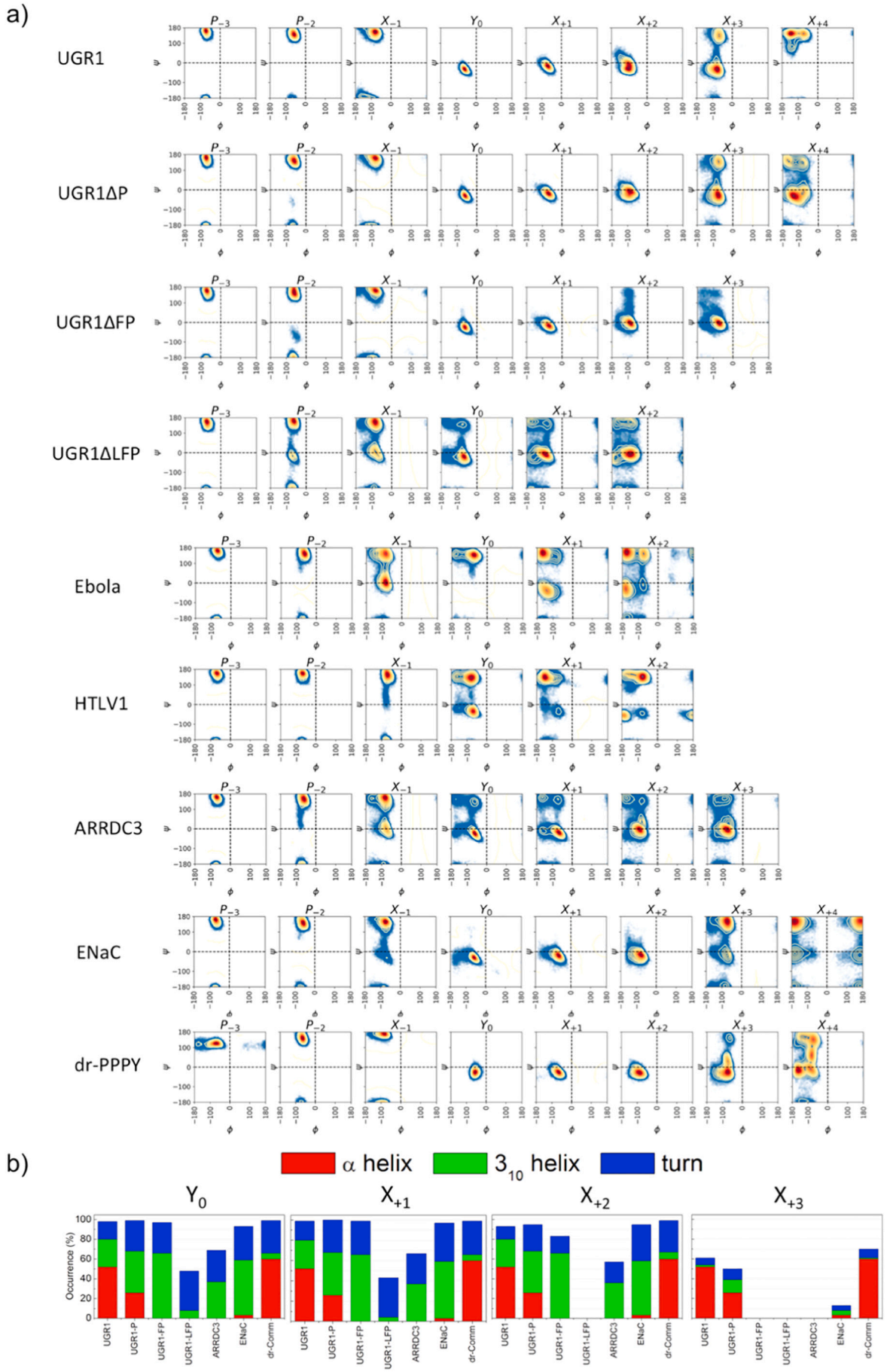

(caption on next page)

Fig. 6. Impact of the C-terminal residues on the conformational preferences of the ligands. **(a)** Ramachandran plots for the ligand residues colored in a rainbow scheme from highly populated (red) to low frequency (blue) conformations. **(b)** Occupancy of the α helix (red), 3_{10} helix (green) and turn (blue) structures at positions Y_0-X_{+3} for the different ligands, calculated with the CPPTRAJ tool in AMBER according to the DSSP algorithm. The Ebola and HTLV1 ligands, showing 0% occupancies in all cases, have not been included in the figure. (For interpretation of the references to colour in this figure legend, the reader is referred to the web version of this article).

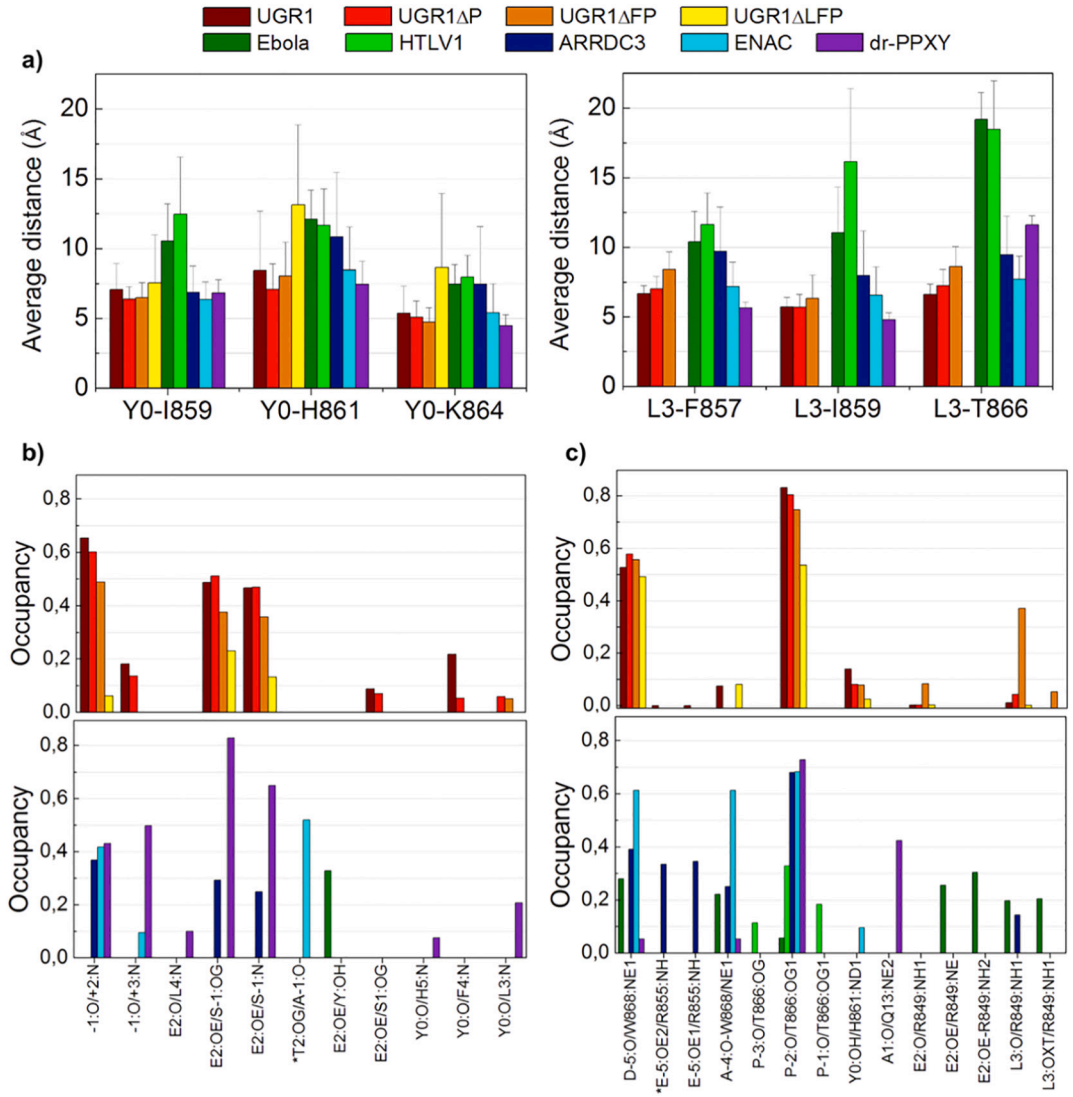

Fig. 7. Molecular dynamics analysis of the interactions established within the NEDD4-WW3 complexes. The different ligands are colored according to the scheme: UGR1 (wine), UGR1ΔP (red), UGR1ΔFP (orange), UGR1ΔLFP (yellow), Ebola (dark green), HTL.1 (light green), ARRDC3 (navy blue), ENaC (cyan) and dr-PPPY (purple) ligands. **(a)** Average distance between the Y_0 and X_{+3} residues in the ligand and the xY (left panel) and xL (right panel) pockets. Shown are the calculated distances between the residue centroids averaged throughout the trajectory together with the corresponding standard deviations (error bars). **(b)** Frequency of occurrence of the intra-molecular hydrogen bonds in the different ligands. **(c)** Frequency of occurrence of inter-molecular hydrogen bonds between the NEDD4-WW3 domain and the different ligands. Shown are the interactions with occupancies >5%. Upper panels include the data for UGR1 and its truncated variants, while the other ligands are shown in the lower panels. Those ligands residues differing in sequence with respect to UGR1 have been noted with an * symbol. (For interpretation of the references to colour in this figure legend, the reader is referred to the web version of this article).

The VLP experiments also demonstrate that these high-affinity peptides, identified against the isolated NEDD4-WW3 domain, effectively interfere with the interactions between the full-length proteins (human NEDD4 and the viral VP40 matrix protein) in a cellular setup, inhibiting budding in Ebola and Marburg viral models and live VSV virus. Previous reports have described the identification and optimization of small-molecule inhibitors of the NEDD4/VP40 interaction through virtual screening against the NEDD4-WW3 domain structure [11,13,55]. The identified compounds showed good antiviral activity in cellular assays and against live virus, but the actual interaction with the NEDD4-WW3 domain was not experimentally established. We present here direct biophysical evidence that blocking the WW domain binding site impedes the NEDD4/VP40 interaction in a cellular setup, and confirm that high-affinity ligands of the isolated NEDD4-WW3 domain are good starting points for the development of antivirals. Because of their peptidic nature, the UGR ligands present several drawbacks (low oral bioavailability, limited stability to proteolytic enzymes, poor bio-distribution, risk of immunogenic effects, as well as high production costs) that hinder their therapeutic application. In the search for broad-spectrum antivirals for early intervention against new viral outbreaks, typically

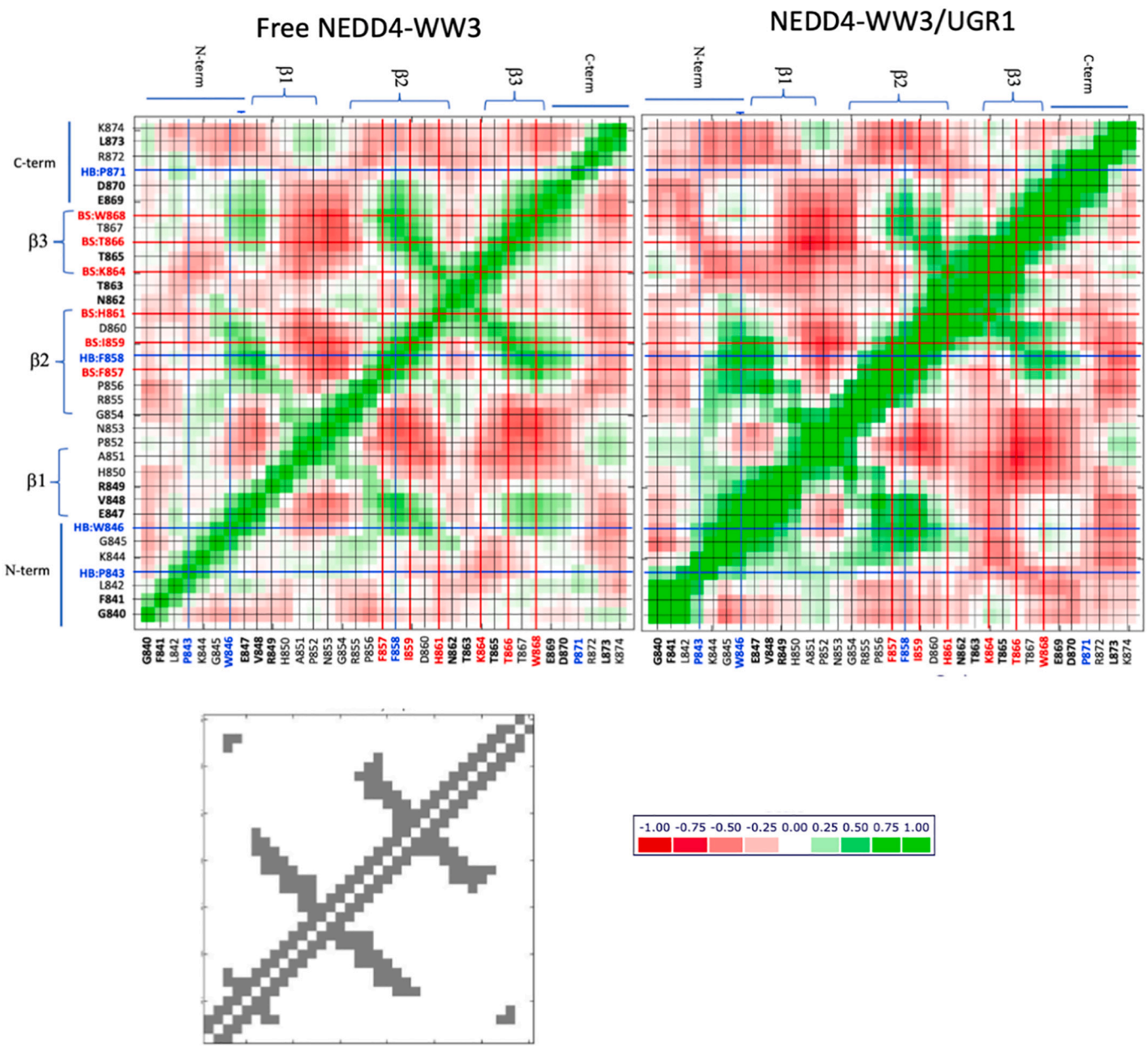

Fig. 8. NMA residue-residue cross-correlation matrices between residue fluctuations. Shown are the raw correlation values for each pair of residues in the WW domain for the free NEDD4-WW3 domain (left panel) and the NEDD4-WW3/UGR1 complex (right panel). Each position is colored with a white to green gradient for positively correlated pairs (moving in the same direction) and white to red gradient for anti-correlated pairs. Residues conforming the binding site and the stabilizing hydrophobic buckle are marked by red ables and red lines and by blue abels and blue lines, respectively. For comparison, the lower panel shows the 2D connectivity map, where each dot represents a spring connection between two residues in the calculations. (For interpretation of the references to colour in this figure legend, the reader is referred to the web version of this article.)

occurring in developing countries, cheaper and orally bioavailable drugs would be desirable. Nonetheless, the high affinity UGR peptides are good starting points for the development of peptidomimetic derivatives. These peptides are also of interest as tools to study the cellular effects of altering NEDD4-WW3 recognition and to develop/optimize high throughput strategies, where they could be used as competitive tracers to screen for potent inhibitors of NEDD4-WW3 interactions. Finally, fluorescent conjugates of the UGR peptides could also be of interest to improve the resolution of Fluorescence Polarization assays, extremely dependent on the probe's binding affinity and currently limited by the low binding affinity the natural NEDD4-WW3 ligands [56].

Additionally, the detailed biophysical study of the UGR1 peptide and its variants provides valuable insight into the molecular determinants of high-affinity for NEDD4-WW3, which are also of general interest for WW domain recognition. Our results show that the nanomolar binding affinity of the UGR peptides is associated with a bulky and rigid FP moiety at the C-terminus of the ligand that elicits remarkable energetic effects without contacting the NEDD4-WW3 domain. In fact, structure-based calculations of the intrinsic binding enthalpy (associated with the direct interactions at the binding interface [57]) do not account for the large reduction in binding enthalpy produced by the removal of the LFP motif ($\Delta\Delta H_{UGR1\text{-}UGR1\Delta LFP} = -37$ kJ·mol^{-1}). On the contrary, opposing the experimental observations, the intrinsic binding enthalpy predicted for the UGR1 ligand is smaller than that calculated for the UGR1ΔLFP truncated variant, due to the apolar area contributed by the LFP motif (see Table S2). The structure-based calculations also fail to account for

the large increment in binding heat capacity induced by the -LFP triad ($\Delta\Delta Cp_{UGR1\text{-}UGR1\Delta LFP}$ = -1.2 kJ·K^{-1} mol^{-1}), even though ΔCp values are generally predicted from structure with high accuracy [58]. These discrepancies are in agreement with numerous reports indicating that WW binding, and, in general, polyproline recognition by protein interaction modules, cannot be well understood attending exclusively to the direct contacts of the interacting surfaces [30,59], and support the idea that conformational effects play a major role in WW recognition [20].

In agreement with this idea, the MD analysis shows that the presence of the bulky and conformationally constrained $F_{+4}P_{+5}$ dyad facilitates the adoption of helical conformations in the Y_0-L_{+3} region, which are further stabilized by capping-like interactions implicating backbone and sidechain atoms of residues S_{-1} and E_{+2} (Fig. 7B). These two features seem to act synergically to achieve submicromolar binding. The same hydrogen bonding pattern is observed for the helix-forming ARRDC3, ENaC, and dr-Comm natural sequences, but does not suffice for tight binding in the absence of the -LFP motif, which is required to achieve high occupancies for the capping interactions in the UGR1 variants (Fig. 7B). Also, for the constraining effect of the -LFP motif to efficiently translate into high binding affinity, strong helical tendencies at Y_0-L_{+3} region seem to be required. In fact, the elongation of the linear Ebola Late domain peptide to include an equivalent -$I_{+4}YP_{+6}$ motif present in the natural Eb-VP40 sequence (ILPTAPPEY$_0$MEA$_{+3}$IYP) only induces a small improvement in binding affinity (Table 1), probably due to the electrostatic repulsion between the two glutamic side chains at positions -1 and +2, which would hinder helicity in this region.

MD simulations also show that the helical conformations stabilized by the -LFP motif in the UGR1 ligand facilitate the contacts between the domain and the L_{+3} side chain, which, in turn, modulate packing of the $P_{-2}PxY_0$ core motif at the binding site (Fig. 7). This is in agreement with the strong differences in NMR-CSP values between the UGR ligands and the ΔLFP truncated variants observed for residues binding site residues F_{857}, I_{859}, and T_{866} (Fig. 3). In fact, for the set of NEDD4-WW3 complexes studied here, the % of occupancy of Y_0-L_{+3} helical (α + 3_{10}) conformations in the MD trajectories strongly correlates to a) the average packing distance of Y_0 at the xY pocket (R = 0.94) (Fig. 9A); b) the formation of the P_{-2}:O/T_{866}:OG intermolecular hydrogen bond (R = 0.93), observed with varying frequencies and lengths in all ligands, excluding the Ebola and HTLV Late domain peptides (Fig. 9B); and c) the average contact distance between L_{+3} and T_{866} (R = 0.89) (Fig. 9C). A weaker correlation and higher dispersion are, nonetheless, observed for the D_{-5}:O/W_{868}:NE1 hydrogen bond at the xP pocket (R = 0.71) (Fig. 9D).

Moreover, our results consistently indicate that the impact of the -LFP triad goes beyond the mere strengthening of the direct interactions at the binding site pockets. In previous studies we have shown that binding of the isolated PPPY motif elicits a high percentage of the experimental binding enthalpy (between 50 and 70%), suggesting that a good part of the conformational reorganization induced by ligand binding is caused by the insertion of the core motif in the xP and xY pockets [20]. This parallels the situation described for SH3 domains, in which the stacking of the xP moieties between the aromatic side chains lining the two conserved xP pockets at the binding site (in a configuration much similar to the xP pocket in WW domains) has been shown to

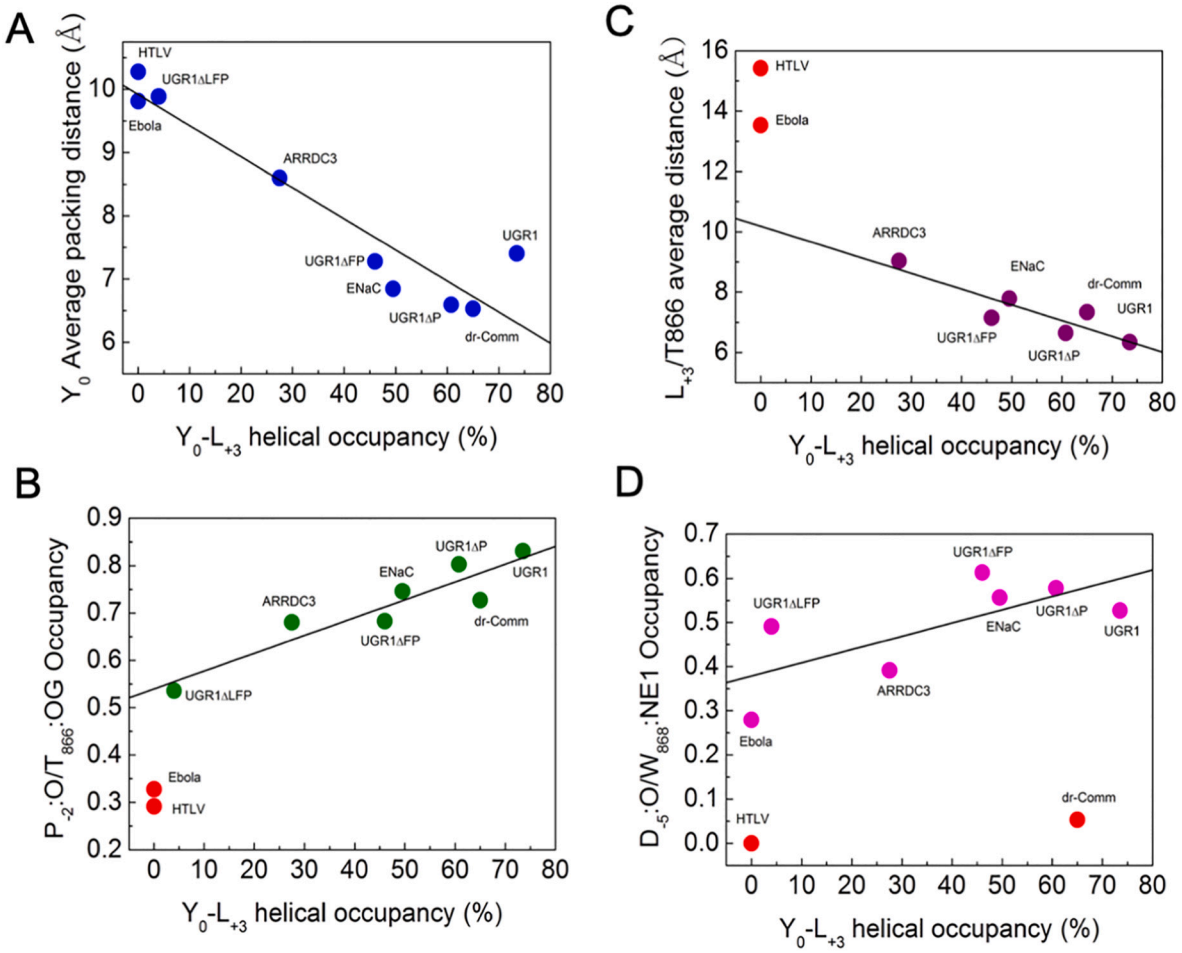

Fig. 9. Correlation between the occupancy of Y_0-L_{+3} helical conformations (α + 3_{10}) in the MD trajectories and A) the average packing distance of Y_0 at the xY pocket; B) the frequency of occurrence of the P_{-2}:O/T_{866}:OG intermolecular hydrogen bond; C) the average contact distance between L_{+3} and T_{866} and D) the frequency of occurrence of the D_{-5}:O/W_{868}:NE1 hydrogen bond at the XP pocket.

perturb the hydrogen bond network throughout the domain, transmitting the binding site perturbation in a domino-like fashion to distant regions in the domain, and contributing to the large enthalpic changes associated to polyproline binding to SH3 domain [32,60]. The experimental and computational results presented here paint a similar picture for the NEDD4-WW3 domain: ligand binding has a strong impact on the domain conformational behavior, modulating intramolecular interactions, dynamics, and cooperativity. These effects are magnified by the presence of the -LFP motif which alters the intramolecular hydrogen bond network, the packing interactions at the hydrophobic buckle, and the overall dynamics of the WW domain, enhancing cooperativity and eliciting strong energetic effects.

In agreement with this idea, a remarkable correlation is also observed between the helical content of the ligands and the experimental binding Gibbs energy (Fig. 10A) as well as the conformational contributions to the binding enthalpy (ΔH_{conf}) calculated from structure (Fig. 10B) ($R = 0.97$ and $R = 0.93$ respectively). A weaker correlation is found for the experimental binding enthalpies, which show a larger dispersion (Fig. 10C). This further sustains the idea that the improvement in binding affinity and binding enthalpies associated to the -LFP motif arise from conformational effects. The ENaC ligand is a clear outlier in these correlations, since, despite its high helical content, it presents moderate values of binding affinity and binding enthalpy. Interestingly, the interaction pattern for this ligand differs from the other complexes: the S_{-1}-E_{+2} capping interactions are substituted by a single hydrogen bond between A_{-1}:O and T_{+2}:Oγ that induces different conformational preferences at T_{+2} and stronger hydrogen bonds between W_{868} and the N-terminal region of the ligand (see Figs. 6 and 7). This observation, together with the fact that no strong preferences were found for the N-terminal positions in the phage display screening, further highlights the importance of the C-terminal region of the peptides and their interaction with residues T_{866} and I_{859} to achieve high affinity against NEDD4-WW3.

In summary, our competitive phage display set-up has allowed us to exploit the high flexibility and low cooperativity characteristic of the NEDD4-WW3 domain to achieve high binding affinity, an unattainable task by rational design. The resulting sequences (UGR1 and UGR2 ligands) can overcome one of the major obstacles in rational design (the strong enthalpy/entropy compensation effects associated with low-affinity interactions and coupled folding/binding equilibria) producing improvements in binding affinity up to 2 orders of magnitude. In agreement with previous studies with natural ligands [20,38], our results confirm that binding of these high-affinity ligands drastically narrows the wide and conformationally heterogeneous native state ensemble of the free NEDD4-WW3 domain, inducing a marked increase in cooperativity. We find that the two synergic features selected by phage display (-1/+2 capping interactions and the C-terminal -LFP motif) produce ligands that modulate the NEDD4-WW3 conformational distribution more efficiently than natural sequences, inducing larger changes in dynamics and cooperativity. Through indirect conformational effects, the UGR peptides elicit remarkable energetic responses resulting in extremely large changes in binding enthalpy and heat capacity, a thermodynamic characteristic of coupled folding/binding equilibrium in intrinsically disordered systems [61]. The UGR1 values almost double in magnitude those obtained for the natural sequences and the UGR truncated variants, further sustaining the idea that the -LFP

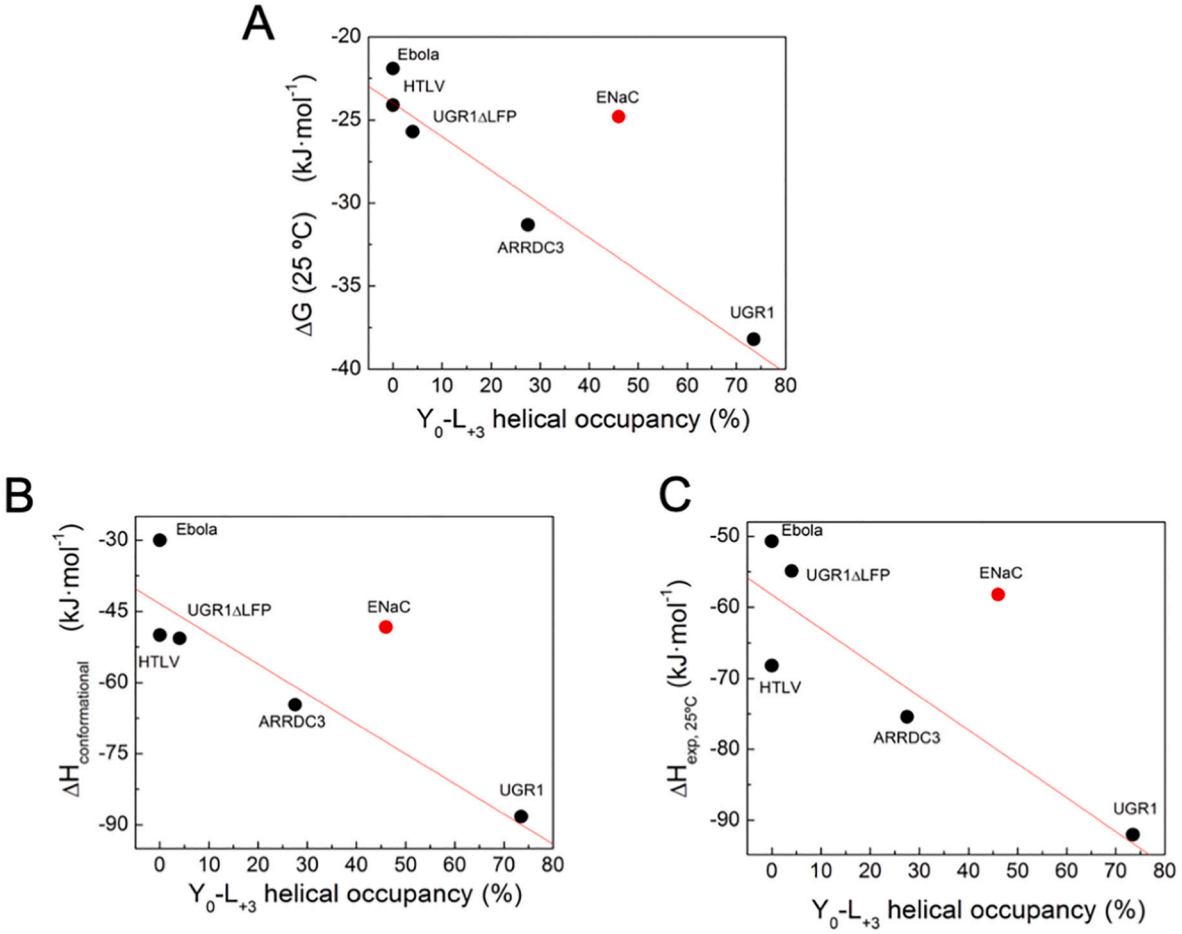

Fig. 10. Correlation between the occupancy of Y_0-L_{+3} helical conformations (α + 3_{10}) in the MD trajectories and A) the experimental binding Gibbs energy; B) the conformational contributions to the binding enthalpy derived from structure-based calculations shown in Table S2; C) the experimental binding enthalpies.

motif enhances the conformational redistribution of the NEDD4-WW3 domain.

Moreover, by combining irrational phage-display approaches with a detailed biophysical characterization of the system we have been able to identify specific and very localized features in the ligand (the -LFP triad) and the NEDD4-WW3 domain (residues T_{866} and I_{859}) that play a pivotal role for tight binding. These two residues, which delimit the xP and xY binding pockets, had been identified in previous studies as key elements for the binding site plasticity observed in WW domain complexes. In fact, the analysis of the structural/energetic database of WW-domain complexes revealed that the best ligands, showing low micromolar binding, systematically induced a specific conformer on the I_{859} side chain [20]. In agreement with this scenario, the different experimental and computational studies of UGR1 binding presented here consistently highlight the role of T_{866} as a key element to achieving binding affinity through optimized interactions at the xP, xY, and especially at the xL pocket. The interplay between T_{866} and I_{859} has also emerged from our analysis as an important feature for the efficient propagation of binding effects throughout the domain. These results pave the way for the development of highly focused virtual screening campaigns to identify non-peptide inhibitors with the right choice of rigid scaffolds mimicking the conformational properties and interaction patterns found to be key for high-affinity against NEDD4-WW3, in search for novel and improved broad-spectrum antivirals as well as potential therapeutic agents for the treatment of cancer, hypertension or neural disorders.

4. Materials and methods

4.1. Protein expression and purification

The NEDD4-WW3 (residues 834 to 878 from isoform 1 of human NEDD4 protein; UniProtKB code P46934) was expressed in *E. coli* BL21/DE3 cells as N-terminal His-tag-GST fusion protein with a TEV protease restriction site engineered between the WW domain and the His-tag-GST. The expression and purification protocols for unlabelled and uniformly labelled ^{15}N NEDD4-WW3 have been previously described in detail [37,62]. Briefly, the over-expressed fusion protein was purified from the soluble fraction of the cell lysate by nickel affinity chromatography. For phage display studies, protein-containing fractions were diluted down to 2 μM in PBS buffer pH 7.4 with 1 mM DTT, frozen in liquid nitrogen and stored at -80 °C. For ITC and NMR studies the GST-His-tag was removed by controlled hydrolysis with recombinant TEV protease and subjected to a second nickel affinity chromatography step followed by a gel filtration on a HiLoad Superdex 75 column (GE healthcare Life Science). The purified isolated domain was concentrated up to 2 mg·mL^{-1} in 40 mM sodium phosphate pH 7.0, frozen in liquid nitrogen and stored at -80 °C. The purity and integrity of the proteins were checked by SDS-Page and mass spectrometry (Mass Spectrometry Service of the CIC at the University of Granada) and estimated to be above 99%.

4.2. Peptide ligands

Synthetic peptides were purchased from JPT (Berlin, Germany). Peptides used for competitive ELISA and ITC were acetylated and amidated at their N- and C-termini, respectively. The Tat-tagged peptides used for the *in vivo* assays were synthesized with free N- and C-termini. In all cases, peptides were synthesized in the solid phase and their molecular masses were confirmed by mass spectrometry. Peptide purity was assessed by analytical HPLC and confirmed to be >98%.

4.3. Nomenclature and systematic notation

The different residues in the peptide ligands were numbered taking the most relevant position (the tyrosine residue in the PPxY motif) as zero, according to the standard notation in [63]. Residues N-terminal from this position follow a negative progression whereas residues C-terminal are denoted by positive numbers. The NEDD4-WW3 domain was numbered according to the full-length isoform 1 of human NEDD4 protein registered at the UniProtKB (code P46934), ranging from the N-terminus position 834 to the C-terminus position 878.

4.4. Protein and peptide concentrations

Protein concentration was measured by absorbance at 280 nm using molecular weights of 34,410 Da (GST-NEDD4-WW3) or 5568 Da (NEDD4-WW3), and extinction coefficients of 54,490 $cm^{-1}\cdot M^{-1}$ and 11,380 $cm^{-1}\cdot M^{-1}$, respectively, determined as described by Gill & von Hippel [64]. Peptide concentration was determined by absorbance at 278 nm using an extinction coefficient of 1450 $M^{-1}\cdot cm^{-1}$ per Tyr residue.

4.5. Phage display

The multivalent pVIII library was generated using the pRSTOP4 phagemid as template and monovalent pIII libraries were based on the pS2202d phagemid. Phagemid templates were kindly provided by Dr. Sachdev Sidhu (University of Toronto).

The pVIII-x_{12} gene library encoding random dodecapeptides was fused to the phagemid region coding for the N-terminus of the gene-8 major coat protein of M13 phage and electroporated for 5 milliseconds in SS320 electrocompetent cells according to the protocol described in here [41]. The resulting library of $\sim 10^{11}$ unique members was purified and screened for three rounds against the target GST-tagged protein, the GST-NEDD4-WW3 domain, by following a standard procedure for the identification of binding motifs for Peptide Recognition Modules (PRM) described in detail here [21,41].

In short, standard rounds began by immobilizing 100 μL per well of the target protein, at 2 μM concentration in Phosphate Saline Buffer (PBS) pH 7.4, overnight and at 4 °C, on a Maxisorp 96-wells plate (M9410-1CS, NUNC ®); the rest of the selection round was performed at room temperature. Second, the plate was blocked with 200 μL per well of PBS supplemented with BSA, and incubated for 1 h, before the binding step was performed. The remaining steps of the selection round were performed with gentle orbital shaking. 100 μL per well of the phage pool was subsequently added and left to incubate for 2 h with the target protein. Weak and non-specific binders were removed after by 3 consecutive washes with 200 μL per well of PBS-Tween20. Specific phage binders were eluted by adding 100 μL per well of 0.1 M HCl and then neutralized by adding a basic solution of Tris-HCl 1 M. To perform the next selection cycle, eluted phages at neutral pH were amplified by an overnight infection of a culture of XL1-Blue E.Coli (200,249, Agilent®) once the OD_{600nm} reached 0.6, in the presence of a M13 Helper Phage (M13KO7 Helper Phage, New England Biolabs), and Ampicillin and Kanamycin as selection antibiotics. These protocols have been described in detailed elsewhere [41].

The top-scoring 25 peptide-phage clones were identified by phage-ELISA as described in [41]. Briefly, for standard phage ELISA, 30 μL per well of a 2 μM solution of either the GST-tagged NEDD4-WW3 domain (positive control), or the GST alone (negative control), were immobilized overnight and at 4 °C on a 384-wells Maxisorp plate; the rest of the assay steps were carried at room temperature. Each well was subsequently blocked with 60 μL of PBS-BSA for 1 h, and then 30 μL of individual supernatants from each phage clone were incubated in duplicate, against the target protein and the negative control, for 2 h with shaking. After washing with 60 μL of PBS-Tween20 for 3 times, specific primary anti-M13-HRP monoclonal (GE life sciences®) at 1:1000 and reagents from TMB substrate kit (Pierce ®) were sequentially added, according to manufacturer's standard protocols, and as described in [41]. Finally, absorbance readings at 450 nm were performed in a Tecan Infinite® plate reader.

The peptide-encoding regions of the respective top 25 clones presenting maximal positive control/negative control absorbance ratios

were then amplified by PCR using a Phusion High Fidelity DNA polymerase (NEB), whose amplicon was further confirmed by gel electrophoresis, and subsequently purified with the ExoSAP-IT kit (Affimetrix) before a final DNA sequencing step.

The pIII-x_5(L/P)P(S/T)Yx_5 and the pIII-x_5(L/P)P(S/T)xxLFP phage libraries were fused to the region of the pSS202d phagemid coding for the N-terminus of the gene-3 protein of M13. Following the standard procedure described above, a pIII-x_5(L/P)P(S/T)Yx_5 library was produced at a variability of $\sim 10^{10}$ members, which was then screened for four standard rounds against 2 μM GST-NEDD4-WW3 as described above.

For the more constrained pIII-x5(L/P)P(S/T)xxLFP library, a library of $\sim 10^9$ members was screened for six selection/amplification rounds. For this, the round 3 amplified phage pool was split in two aliquots, which were screened under two parallel protocols of incremental stringencies, requiring the following modifications from rounds 4 to 6. *Protocol A*: A phage aliquot was incubated for 2 h against half the concentration of immobilized GST-NEDD4-WW3, 1 μM concentration, following the rest of the standard selection/amplification procedure. Such modified selection cycle was repeated for two extra rounds, from where individual phage-binders were isolated and assayed by ELISA (see below). *Protocol B*: An additional step was added before the incubation of the phage-binding pool with respect to Protocol A. For this, 200 μL per well of an equimolar solution of the high-affinity peptide P53BP2 was pre-incubated with the same stock of GST-NEDD4-WW3 at 1 μM concentration while immobilizing. P53BP2 leftovers were then washed-off, and the corresponding phage aliquot was subsequently incubated and screened following the standard protocol. This modified selection cycle was equally repeated for two extra rounds in parallel to protocol A.

In order to compare the outcomes from protocols A and B, the standard phage ELISA described above was modified in a two-steps assay workflow. 1) Individual phage clones from each round were amplified and their corresponding supernatants were tested for specific binding against 1 μM of immobilized GST-NEDD4-WW3, following the rest of the standard ELISA protocol. 2) Top scoring ELISA binders from step one were then re-assayed against 1 μM of GST-NEDD4-WW3/P53BP2 complex, which was immobilized as in stringent selection rounds from Protocol B. From the binding incubation step, the rest of the ELISA followed the standard procedure. Finally, absorbance ratios were compared for each phage clone supernatant in the absence and in the presence of the P53BP2 competing agent.

4.6. Virus-like-particle (VLP) budding assays

BHK-21 and HEK293T cells were maintained in Dulbecco's modified Eagle's medium (DMEM) supplemented with 10% fetal calf serum (FCS), penicillin (100 $U \cdot ml^{-1}$)/streptomycin(100 $g \cdot ml^{-1}$) at 37 °C in a humidified 5% CO2 incubator. Anti-VSV-M monoclonal antibody 23H12 was kindly provided by D. Lyles (Winston-Salem, NC); anti-flag monoclonal antibody was purchased from Sigma-Aldrich. VSV WT virus was propagated in BHK-21 cells as described previously [50].

VLP assays were performed in HEK293T as previously described [11] using eVP40 or mVP40 expression plasmids and incubating the transfected cells with 10 to 30 μM YGRKKRRQRRRRPPQ-LDSLPSYSELFP (Tat-UGR2) peptide. The isolated Tat-tag [YGRKKRRQRRRRPPQ] and the Tat-Tagged p41 peptide, a proline-rich ligand of the Abl-SH3 domain, [YGRKKRRQRRRRPPQ-APSYPPPPPP] were used as negative controls.

The effect of Tat-UGR2 on the release of Vesicular Stomatitis Virus (VSV-WT) was studied in HEK293T cells as described before [55], incubating the VSV-infected cells for 4 h with 10 or 30 μM of the Tat-tagged peptides.

4.7. Isothermal titration calorimetry

ITC experiments were performed with a high-precision ITC-200 titration calorimeter (Microcal Inc., Northampton, Massachusetts) as described before [20]. To minimize ionization effects from the buffer, all titrations were performed in 20 mM sodium phosphate buffer, pH 7.0, 25 °C. In most cases, 1 μL of peptide solution at 300–800 μM was titrated into the calorimetric cell containing the protein at 30–45 μM. For UGR1-ΔLFP titrations, showing lower affinity, higher protein and peptide concentrations were used (40 μM and 1.5 mM respectively) and a profile of injection volumes from 0.5 to 5 μL was devised to better define the titration curve. The heat evolved after each injection was obtained from the integral of the calorimetric signal. The heat associated with the binding process was calculated as the difference between the heat of reaction and the corresponding heat of dilution, obtained from independent titrations of the peptides into the buffer. The resulting binding isotherms were analyzed by non-linear least-squares fittings to a model corresponding to a single set of identical sites, as described before [26].

4.8. Nuclear magnetic resonance

^1H—^{15}N correlation spectra were recorded at 15 °C on a Varian NMR Direct-Drive System 600 MHz Spectrometer (1H frequency of 600.25 MHz). Experiments were recorded in 90% H_2O/10% D_2O, 20 mM potassium-phosphate buffer pH 7 with a protein concentration of 245 μM and increasing amounts of the ligands. The protein to ligand ratios used during the titrations were 1:0, 1:0.25, 1:0.5, 1:1, 1:2, 1:3 and 1:5. Protein backbone resonance assignments were obtained as previously described [20]. NMR spectra were processed using NMRPipe [65], and analyzed using the SPARKY [66] and XEASY [67] programs. ^{15}N and ^1H chemical shift perturbations (ΔδN) of each amide were calculated from the corresponding pair of differential (bound-unbound) chemical shifts of the proton (ΔδH) and the nitrogen (ΔδN) by using the following equation:

$$\Delta\delta HN = (([\Delta\delta H]2 + [\Delta\delta N/6.51]2\,))1/2 \quad (1)$$

4.9. Model building and molecular dynamics

The X-ray structure of the NEDD4-WW3 domain bound to peptide ARRDC3 (PDB ID: 4N7H) [23] was used as a template to build the model structure of the UGR1 peptide by replacing residues of ARRDC3 with the corresponding amino acids in UGR1 using the design tools in Discovery Studio 2.1 Suite (Accelrys Software Inc.). The resulting structures were subjected to subsequent refinement using the FlexPepDock webserver [68].

MD simulations were produced using AMBER14 [69] and the ff03 force field [70]. The starting structures were solvated in a truncated octahedron box of water, and counter-ions were added to neutralize the charges. The system was then minimized with a harmonic restraint at the protein atoms for 2000 steps. Finally, the full system was equilibrated. All trajectories were generated at a constant temperature (298 K) and pressure (1 atm), under periodic-boundary conditions. Electrostatic interactions were computed using the Particle Mesh-Ewald algorithm with a real-space cut-off distance of 12 Å for the van der Waals interactions. The Langevin scheme was used to control temperature and pressure. MD trajectories were recorded every 2 ps. Three independent 50 ns replicas were generated for each complex structure that were combined in to a single 150 ns trajectory and analyzed using AmberTools 14 and CPPTRAJ commands considering the default threshold for hydrogen bond formation and the DSSP algorithm for secondary structure assignment. Inter-residue distances were calculated as the distances between the center of mass of the corresponding side chains.

4.10. Coarse grained normal mode analysis

Coarse-grained normal mode analysis (NMA) based on Elastic Network Models derived from structure (ENM) [53,54] was performed using the FlexServ (http://mmb.irbbarcelona.org/FlexServ/) [53] and

Dynomics (http://dynomics.pitt.edu/) packages [54]. The UGR1 and UGR1ΔLFP modeled structures were used for the calculations. For the free domain two options were considered that rendered equivalent results: the X-ray structure of the unliganded NEDD4-WW3 (chain A in 4N7F pdb file) and the domain structure extracted from the model complexes. FlexServ calculations were performed with a mixed formalism based on the multiparametric fitting of NMA to atomistic MD simulations, using default parameters [71]. The Dynomics calculations were performed with a cutoff for ANM modes of 15 Å, producing a total of 20 slow modes that were subsquently considered for the analysis. The two algorithms produced consistent cross-correlation matrices for the different structures. Dynomics allows the identification of sensors and effectors based on the Perturbation-Response-Scanning method adapted to GNM. A response matrix was generated using the 20 slowest modes in which the i^{th} element provides a measure of the sensitivity of node i to perturbation at node j [72].

CRediT authorship contribution statement

Francisco Castillo: Investigation, Methodology, Visualization, Formal Analysis, Writing-Original Draft preparation, Writing-Review & Editing. **Carles Corbi-Verge:** Investigation, Formal Analysis, Writing-Original Draft preparation, Writing-Review & Editing. **Javier Murciano-Calles:** Methodology, Writing-Review & Editing. **Adela M. Candel:** Investigation, Formal Analysis, Visualization, Writing-Review & Editing. **Ziying Han:** Investigation, Visualization, Writing-Review & Editing. **Manuel Iglesias-Bexiga:** Investigation, Formal Analysis, Writing-Review & Editing. **Javier Ruiz-Sanz:** Investigation, Formal Analysis, Writing-Review & Editing. **Philip Kim:** Resources, Writing-Review & Editing. **Ronald N. Harty:** Investigation, Resources, Visualization, Writing-Review & Editing, Funding acquisition. **Jose C. Martinez:** Supervision, Project administration, Formal Analysis, Writing-Original Draft preparation, Writing-Review & Editing. **Irene Luque:** Conceptualization, Investigation, Supervision, Writing-Original Draft preparation, Writing-Review & Editing, Visualization, Project administration, Funding acquisition.

Declaration of competing interest

The authors declare that they do not have conflicts of interest.

Acknowledgements

This research has been financed by grants BIO2016-78746-C2-1-R and PID2020-112895RB-100 from the Spanish Ministry of Education and Science (I.L.) including AEI/FEDER EU funds. R.N.H. was funded in part by National Institutes of Health grants AI138052 and AI138630. M. I.B. and J.M.C. were recipients of a research contract from the Spanish Ministry of Education and Science. F.C. was funded by a predoctoral fellowship from the Andalusian Government P10-CVI-5915. J.M.C. acknowledges a reincorporation research contract from the University of Granada. We thank Dr. Sachdev Sidhu for his invaluable assistance setting up the phage display techniques in our laboratory. We also thank the support of the C.I.C. of the University of Granada.

Appendix A. Supplementary data

Supplementary data to this article can be found online at https://doi.org/10.1016/j.ijbiomac.2022.03.010.

References

[1] Z. Salah, A. Alian, R.I. Aqeilan, WW domain-containing proteins: retrospectives and the future, Front. Biosci. (Landmark Ed.) 17 (2012) 331–348.
[2] N.S. Chang, R. Lin, C.I. Sze, R.I. Aqeilan, Editorial: WW domain proteins in signaling, cancer growth, neural diseases, and metabolic disorders, FrontOncol. 9 (2019) 719.
[3] S.S. Huang, L.J. Hsu, N.S. Chang, Functional role of WW domain-containing proteins in tumor biology and diseases: insight into the role in ubiquitin-proteasome system, FASEB Bioadv. 2 (4) (2020) 234–253.
[4] G. Novelli, J. Liu, M. Biancolella, T. Alonzi, A. Novelli, J.J. Patten, D. Cocciadiferro, E. Agolini, V.L. Colona, B. Rizzacasa, R. Giannini, B. Bigio, D. Goletti, M. R. Capobianchi, S. Grelli, J. Mann, T.D. McKee, K. Cheng, F. Amanat, F. Krammer, A. Guarracino, G. Pepe, C. Tomino, Y. Tandjaoui-Lambiotte, Y. Uzunhan, S. Tubiana, J. Ghosn, L.D. Notarangelo, H.C. Su, L. Abel, A. Cobat, G. Elhanan, J. J. Grzymski, A. Latini, S.S. Sidhu, S. Jain, R.A. Davey, J.L. Casanova, W.Y. Wei, P. P. Pandolfi, C.H.G. Effort, , FCCS Group, C.-C. Cohort, Inhibition of HECT E3 ligases as potential therapy for COVID-19, Cell Death Dis 12 (4) (2021).
[5] N.A. Boase, S. Kumar, NEDD4: the founding member of a family of ubiquitin-protein ligases, Gene 557 (2) (2015) 113–122.
[6] M. Scheffner, S. Kumar, Mammalian HECT ubiquitin-protein ligases: biological and pathophysiological aspects, Biochim. Biophys. Acta 1843 (1) (2014) 61–74.
[7] H. Abriel, J. Loffing, J. Rebhun, J. Pratt, L. Schild, J.D. Horisberger, D. Rotin, O. Staub, Defective Regulation of the Epithelial Na+ Channel by NEDD4 in Liddle's Syndrome, 1999.
[8] X. Ye, L. Wang, B. Shang, Z. Wang, W. Wei, NEDD4: a promising target for cancer therapy, Curr. Cancer Drug Targets 14 (6) (2014) 549–556.
[9] P.D. Bieniasz, Late budding domains and host proteins in enveloped virus release, Virology 344 (1) (2006) 55–63.
[10] E.O. Freed, Viral late domains, J. Virol. 76 (10) (2002) 4679–4687.
[11] Z. Han, J. Lu, Y. Liu, B. Davis, M.S. Lee, M.A. Olson, G. Ruthel, B.D. Freedman, M. J. Schnell, J.E. Wrobel, A.B. Reitz, R.N. Harty, Small-molecule probes targeting the viral PPxY-host Nedd4 interface block egress of a broad range of RNA viruses, J. Virol. 88 (13) (2014) 7294–7306.
[12] R.N. Harty, No exit: targeting the budding process to inhibit filovirus replication, Antivir. Res. 81 (3) (2009) 189–197.
[13] Z. Han, H. Ye, J. Liang, A. Shepley-McTaggart, J.E. Wrobel, A.B. Reitz, A. Whigham, K.N. Kavelish, M.S. Saporito, B.D. Freedman, O. Shtanko, R.N. Harty, Compound FC-10696 inhibits egress of Marburg virus, Antimicrob. Agents Chemother. 65 (7) (2021), e0008621.
[14] M.J. Macias, S. Wiesner, M. Sudol, WW and SH3 domains, two different scaffolds to recognize proline-rich ligands, FEBS Lett. 513 (1) (2002) 30–37.
[15] J.R. Pires, F. Taha-Nejad, F. Toepert, T. Ast, U. Hoffmuller, J. Schneider-Mergener, R. Kuhne, M.J. Macias, H. Oschkinat, Solution structures of the YAP65 WW domain and the variant L30 K in complex with the peptides GTPPPPYTVG, N-(n-octyl)-GPPPY and PLPPY and the application of peptide libraries reveal a minimal binding epitope, J. Mol. Biol. 314 (5) (2001) 1147–1156.
[16] L.J. Ball, R. Kuhne, J. Schneider-Mergener, H. Oschkinat, Recognition of proline-rich motifs by protein-protein-interaction domains, Angew Chem Int Ed Engl 44 (19) (2005) 2852–2869.
[17] L. Otte, U. Wiedemann, B. Schlegel, J.R. Pires, M. Beyermann, P. Schmieder, G. Krause, R. Volkmer-Engert, J. Schneider-Mergener, H. Oschkinat, WW domain sequence activity relationships identified using ligand recognition propensities of 42 WW domains, Prot. Sci. 12 (3) (2003) 491–500.
[18] J. Kasanov, G. Pirozzi, A.J. Uveges, B.K. Kay, Characterizing class I WW domains defines key specificity determinants and generates mutant domains with novel specificities, Chem. Biol. 8 (3) (2001) 231–241.
[19] A. Zarrinpar, R.P. Bhattacharyya, W.A. Lim, The structure and function of proline recognition domains, Sci. STKE 2003 (179) (2003) RE8.
[20] M. Iglesias-Bexiga, A. Palencia, C. Corbi-Verge, P. Martin-Malpartida, F.J. Blanco, M.J. Macias, E.S. Cobos, I. Luque, Binding site plasticity in viral PPxY late domain recognition by the third WW domain of human NEDD4, Sci. Rep. 9 (1) (2019) 15076.
[21] H. Huang, S.S. Sidhu, Studying binding specificities of peptide recognition modules by high-throughput phage display selections, Methods Mol. Biol. 781 (2011) 87–97.
[22] M. Sudol, C.C. Recinos, J. Abraczinskas, J. Humbert, A. Farooq, WW or WoW: the WW domains in a union of bliss, IUBMB Life 57 (12) (2005) 773–778.
[23] S. Qi, M. O'Hayre, J.S. Gutkind, J.H. Hurley, Structural and biochemical basis for ubiquitin ligase recruitment by arrestin-related domain-containing protein-3 (ARRDC3), J. Biol. Chem. 289 (8) (2014) 4743–4752.
[24] E.J. Dodson, V. Fishbain-Yoskovitz, S. Rotem-Bamberger, O. Schueler-Furman, Versatile communication strategies among tandem WW domain repeats, Exp. Biol. Med. (Maywood) 240 (3) (2015) 351–360.
[25] A.J. Ruben, Y. Kiso, E. Freire, Overcoming roadblocks in lead optimization: a thermodynamic perspective, Chem. Biol. Drug Des. 67 (1) (2006) 2–4.
[26] A. Palencia, E.S. Cobos, P.L. Mateo, J.C. Martinez, I. Luque, Thermodynamic dissection of the binding energetics of proline-rich peptides to the abl-SH3 domain: implications for rational ligand design, J. Mol. Biol. 336 (2) (2004) 527–537.
[27] A. Palencia, A. Camara-Artigas, M.T. Pisabarro, J.C. Martinez, I. Luque, Role of interfacial water molecules in proline-rich ligand recognition by the Src homology 3 domain of Abl, J. Biol. Chem. 285 (4) (2010) 2823–2833.
[28] M. Iglesias-Bexiga, F. Castillo, E.S. Cobos, T. Oka, M. Sudol, I. Luque, WW domains of the yes-kinase-associated-protein (YAP) transcriptional regulator behave as independent units with different binding preferences for PPxY motif-containing ligands, PLoS One 10 (1) (2015), e0113828.
[29] A. Zafra-Ruano, I. Luque, Interfacial water molecules in SH3 interactions: getting the full picture on polyproline recognition by protein-protein interaction domains, FEBS Lett. 586 (17) (2012) 2619–2630.
[30] J.M. Martin-Garcia, J. Ruiz-Sanz, I. Luque, Interfacial water molecules in SH3 interactions: a revised paradigm for polyproline recognition, Biochem. J. 442 (2) (2012) 443–451.

[31] J.C. Ferreon, V.J. Hilser, Thermodynamics of binding to SH3 domains: the energetic impact of polyproline II (PII) helix formation, Biochemistry 43 (24) (2004) 7787–7797.
[32] C. Wang, N.H. Pawley, L.K. Nicholson, The role of backbone motions in ligand binding to the c-Src SH3 domain, J. Mol. Biol. 313 (4) (2001) 873–887.
[33] S. Arold, R. O'Brien, P. Franken, M.P. Strub, F. Hoh, C. Dumas, J.E. Ladbury, RT loop flexibility enhances the specificity of src family SH3 domains for HIV-1 nef, Biochemistry 37 (42) (1998) 14683–14691.
[34] M. Wittekind, C. Mapelli, V. Lee, V. Goldfarb, M.S. Friedrichs, C.A. Meyers, L. Mueller, Solution structure of the Grb2 N-terminal SH3 domain complexed with a ten-residue peptide derived from SOS: direct refinement against NOEs, J-couplings and 1H and 13C chemical shifts, J. Mol. Biol. 267 (4) (1997) 933–952.
[35] G.G. Maisuradze, J. Medina, K. Kachlishvili, P. Krupa, M.A. Mozolewska, P. Martin-Malpartida, L. Maisuradze, M.J. Macias, H.A. Scheraga, Preventing fibril formation of a protein by selective mutation, Proc. Natl. Acad. Sci. 112 (44) (2015) 13549–13554.
[36] M. Szczepaniak, M. Iglesias-Bexiga, M. Cerminara, M. Sadqi, C. Sanchez de Medina, J.C. Martinez, I. Luque, V. Munoz, Ultrafast folding kinetics of WW domains reveal how the amino acid sequence determines the speed limit to protein folding, Proc. Natl. Acad. Sci. U. S. A. 116 (17) (2019) 8137–8142.
[37] M. Iglesias-Bexiga, M. Szczepaniak, C. Sanchez de Medina, E.S. Cobos, R. Godoy-Ruiz, J.C. Martinez, V. Munoz, I. Luque, Protein folding cooperativity and thermodynamic barriers of the simplest beta-sheet fold: a survey of WW domains, J. Phys. Chem. B 122 (49) (2018) 11058–11071.
[38] V. Panwalkar, P. Neudecker, M. Schmitz, J. Lecher, M. Schulte, K. Medini, M. Stoldt, M.A. Brimble, D. Willbold, A.J. Dingley, The Nedd4-1 WW domain recognizes the PY motif peptide through coupled folding and binding equilibria, Biochemistry 55 (4) (2016) 659–674.
[39] V. Panwalkar, P. Neudecker, D. Willbold, A.J. Dingley, Multiple WW domains of Nedd4-1 undergo conformational exchange that is quenched upon peptide binding, FEBS Lett. 591 (11) (2017) 1573–1583.
[40] A. Persaud, P. Alberts, E.M. Amsen, X. Xiong, J. Wasmuth, Z. Saadon, C. Fladd, J. Parkinson, D. Rotin, Comparison of substrate specificity of the ubiquitin ligases Nedd4 and Nedd4-2 using proteome arrays, Mol. Syst. Biol. 5 (2009) 333.
[41] R. Tonikian, Y. Zhang, C. Boone, S.S. Sidhu, Identifying specificity profiles for peptide recognition modules from phage-displayed peptide libraries, Nat. Protoc. 2 (6) (2007) 1368–1386.
[42] X. Espanel, M. Sudol, Yes-associated protein and p53-binding protein-2 interact through their WW and SH3 domains, J. Biol. Chem. 276 (17) (2001) 14514–14523.
[43] E.K. Koepf, H.M. Petrassi, G. Ratnaswamy, M.E. Huff, M. Sudol, J.W. Kelly, Characterization of the structure and function of W –> F WW domain variants: identification of a natively unfolded protein that folds upon ligand binding, Biochemistry 38 (43) (1999) 14338–14351.
[44] R. Bobby, K. Medini, P. Neudecker, T.V. Lee, M.A. Brimble, F.J. McDonald, J. S. Lott, A.J. Dingley, Structure and dynamics of human Nedd4-1 WW3 in complex with the alphaENaC PY motif, Biochim. Biophys. Acta 1834 (8) (2013) 1632–1641.
[45] V. Kanelis, M.C. Bruce, N.R. Skrynnikov, D. Rotin, J.D. Forman-Kay, Structural determinants for high-affinity binding in a Nedd4 WW3* domain-comm PY motif complex, Structure 14 (3) (2006) 543–553.
[46] M.E. Bayer, B.S. Blumberg, B. Werner, Particles associated with Australia antigen in the sera of patients with leukaemia, Down's syndrome and hepatitis, Nature 218 (5146) (1968) 1057–1059.
[47] K.L. Warfield, D.L. Swenson, G. Demmin, S. Bavari, Filovirus-like particles as vaccines and discovery tools, Expert Rev. Vacc. 4 (3) (2005) 429–440.
[48] S. Debaisieux, F. Rayne, H. Yezid, B. Beaumelle, The ins and outs of HIV-1 tat, Traffic 13 (3) (2012) 355–363.
[49] T. Irie, E. Carnero, A. Garcia-Sastre, R.N. Harty, In vivo replication and pathogenesis of vesicular stomatitis virus recombinant M40 containing Ebola virus L-domain sequences, Infect Dis. (Auckl) 5 (2012) 59–64.
[50] T. Irie, J.M. Licata, H.R. Jayakar, M.A. Whitt, P. Bell, R.N. Harty, Functional analysis of late-budding domain activity associated with the PSAP motif within the vesicular stomatitis virus M protein, J. Virol. 78 (14) (2004) 7823–7827.
[51] P.C. Henry, V. Kanelis, M.C. O'Brien, B. Kim, I. Gautschi, J. Forman-Kay, L. Schild, D. Rotin, Affinity and specificity of interactions between Nedd4 isoforms and the epithelial Na+ channel, J. Biol. Chem. 278 (22) (2003) 20019–20028.
[52] A.R. Viguera, J.C. Martinez, V.V. Filimonov, P.L. Mateo, L. Serrano, Thermodynamic and kinetic analysis of the SH3 domain of spectrin shows a two-state folding transition, Biochemistry 33 (8) (1994) 2142–2150.
[53] J. Camps, O. Carrillo, A. Emperador, L. Orellana, A. Hospital, M. Rueda, D. Cicin-Sain, M. D'Abramo, J.L. Gelpi, M. Orozco, FlexServ: an integrated tool for the analysis of protein flexibility, Bioinformatics 25 (13) (2009) 1709–1710.
[54] H. Li, Y.Y. Chang, J.Y. Lee, I. Bahar, L.W. Yang, DynOmics: dynamics of structural proteome and beyond, Nucleic Acids Res. 45 (W1) (2017) W374–W380.
[55] H.M. Loughran, Z. Han, J.E. Wrobel, S.E. Decker, G. Ruthel, B.D. Freedman, R. N. Harty, A.B. Reitz, Quinoxaline-based inhibitors of Ebola and Marburg VP40 egress, Bioorg. Med. Chem. Lett. 26 (15) (2016) 3429–3435.
[56] X. Huang, Fluorescence polarization competition assay: the range of resolvable inhibitor potency is limited by the affinity of the fluorescent ligand, J. Biomol. Screen. 8 (1) (2003) 34–38.
[57] I. Luque, E. Freire, Structural parameterization of the binding enthalpy of small ligands, Proteins 49 (2) (2002) 181–190.
[58] I. Luque, E. Freire, Structure-based prediction of binding affinities and molecular design of peptide ligands, Methods Enzymol. 295 (1998) 100–127.
[59] A. Zafra Ruano, E. Cilia, J.R. Couceiro, J. Ruiz Sanz, J. Schymkowitz, F. Rousseau, I. Luque, T. Lenaerts, From binding-induced dynamic effects in SH3 structures to evolutionary conserved sectors, PLoS Comput. Biol. 12 (5) (2016), e1004938.
[60] F. Cordier, C. Wang, S. Grzesiek, L.K. Nicholson, Ligand-induced strain in hydrogen bonds of the c-Src SH3 domain detected by NMR, J. Mol. Biol. 304 (4) (2000) 497–505.
[61] A. Schon, E. Freire, Binding thermodynamics to intrinsically disordered protein domains, Methods Mol. Biol. 2141 (2020) 449–462.
[62] E.S. Cobos, M. Iglesias-Bexiga, J. Ruiz-Sanz, P.L. Mateo, I. Luque, J.C. Martinez, Thermodynamic characterization of the folding equilibrium of the human Nedd4-WW4 domain: at the frontiers of cooperative folding, Biochemistry 48 (36) (2009) 8712–8720.
[63] R. Aasland, C. Abrams, C. Ampe, L.J. Ball, M.T. Bedford, G. Cesareni, M. Gimona, J. H. Hurley, T. Jarchau, V.P. Lehto, M.A. Lemmon, R. Linding, B.J. Mayer, M. Nagai, M. Sudol, U. Walter, S.J. Winder, Normalization of nomenclature for peptide motifs as ligands of modular protein domains, FEBS Lett. 513 (1) (2002) 141–144.
[64] S.C. Gill, P.H. von Hippel, Calculation of protein extinction coefficients from amino acid sequence data, Anal. Biochem. 182 (2) (1989) 319–326.
[65] F. Delaglio, S. Grzesiek, G.W. Vuister, G. Zhu, J. Pfeifer, A. Bax, NMRPipe: a multidimensional spectral processing system based on UNIX pipes, J. Biomol. NMR 6 (3) (1995) 277–293.
[66] T.D. Goddard, D.G. Kneller, Sparky 3, University of California, San Francisco.
[67] C. Bartels, T.H. Xia, M. Billeter, P. Guntert, K. Wuthrich, The program XEASY for computer-supported NMR spectral analysis of biological macromolecules, J. Biomol. NMR 6 (1) (1995) 1–10.
[68] N. London, B. Raveh, E. Cohen, G. Fathi, O. Schueler-Furman, Rosetta FlexPepDock web server–high resolution modeling of peptide-protein interactions, Nucleic Acids Res 39 (Web Server issue) (2011) W249–W253.
[69] D.A. Case, V. Babin, J.T. Berryman, R.M. Betz, Q. Cai, D.S. Cerutti, T.E. Cheatham, T.A. Darden, R.E. Duke, H. Gohlke, A.W. Goetz, S. Gusarov, N. Homeyer, P. Janowski, J. Kaus, I. Kolossvary, A. Kovalenko, T.S. Lee, S. LeGrand, T. Luchko, R. Luo, B. Madej, K.M. Merz, F. Paesani, D.R. Roe, A. Roitberg, C. Sagui, R. Salomon-Ferrer, G. Seabra, C.L. Simmerling, W. Smith, J. Swalls, R.C. Walker, J. Wang, R.M. Wolf, X. Wu, P.A. Kollman, AMBER 14, University of California, San Francisco, 2014.
[70] J. Ciarkowski, S. Luczak, D. Jagiela, E. Sikorska, J. Wojcik, M. Oleszczuk, J. Izdebski, Ensemble fits of restrained peptides' conformational equilibria to NMR data. Dependence on force fields: AMBER/8 ff03 versus ECEPP/3, J. Mol. Graph Model 32 (2012) 67–74.
[71] L. Orellana, M. Rueda, C. Ferrer-Costa, J.R. Lopez-Blanco, P. Chacon, M. Orozco, Approaching elastic network models to molecular dynamics flexibility, J. Chem. Theory Comput. 6 (9) (2010) 2910–2923.
[72] C. Atilgan, A.R. Atilgan, Perturbation-response scanning reveals ligand entry-exit mechanisms of ferric binding protein, PLoS Comput. Biol. 5 (10) (2009), e1000544.